

# DESIGN OF AN X-RAY CT SYSTEM WITH IMPLEMENTATION OF SPARSE-DATA RECONSTRUCTION

A thesis

Presented to

The academic faculty

By

Luke J Maloney

In partial fulfillment

Of the requirements for the degree

Master of Science in Medical Physics

Georgia Institute of Technology

August 2017

Copyright © Luke James Maloney 2017

# DESIGN OF AN X-RAY CT SYSTEM WITH IMPLEMENTATION OF SPARSE-DATA RECONSTRUCTION

Approved by:

**Dr. Anna Erickson**, Advisor

School of Mechanical Engineering

*Georgia Institute of Technology*

**Dr. Justin Roper**

Department of Radiation Oncology

*Emory University School of Medicine*

**Dr. C-K Chris Wang**

School of Mechanical Engineering

*Georgia Institute of Technology*

Date approved: July 20, 2017

## ACKNOWLEDGMENTS

I would like to thank my advisor, Dr. Anna Erickson, for contributing her time and resources to mentoring me throughout my work. I would also like to thank my committee members, Dr. C-K Chris Wang and Dr. Justin Roper, who have always been ready and willing to answer my questions, help me work through problems, and who have been fantastic mentors during my time at Georgia Tech.

I'd like to thank my colleagues Dr. Paul Rose Jr., Joseph Harms, and Wesley Gillis, who have guided me to understanding in many topics, with great conversation and teaching ability as well as excelling patience.

I would also like to thank my mom and dad, Sherry and Mike. Without their support and inspiration, this work would not have been possible.

## TABLE OF CONTENTS

ACKNOWLEDGMENTS	III
LIST OF TABLES	V
LIST OF FIGURES	VI
LIST OF ABBREVIATIONS	VII
CHAPTER 1 – INTRODUCTION	1
1.1 Importance of x-ray imaging in medical practice	1
1.2 Objectives	4
CHAPTER 2 – BACKGROUND	5
2.1 Principles of x-ray CT imaging and reconstruction	5
2.2 Reconstruction algorithms	14
2.2.1 Filtered backprojection	15
2.2.2 Other analytical techniques	18
2.2.3 Iterative approaches	19
CHAPTER 3 – DESIGN OF X-RAY CT SYSTEM	21
3.1 Equipment and materials	21
3.2 Practical considerations of system design	22
3.2.1 Focal spot penumbra effect	22
3.2.2 Signal-to-noise ratio	23
3.3 Measurement and construction	24
3.3.1 System geometry	28
CHAPTER 4 – RESULTS	30
4.1 Dataset acquisition	30
4.1.1 FBP and ART reconstructions	31
4.1.2 TSVD method and characteristics	35
4.1.3 Tikhonov and TV regularization	38
4.2 Comparison of algorithms	42
CHAPTER 5 – DISCUSSION	46
CHAPTER 6 – CONCLUSION	48
REFERENCES	49

## LIST OF TABLES

TABLE 1. CHARACTERISTICS OF HAMAMATSU L9631 X-RAY SOURCE	21
TABLE 2. CHARACTERISTICS OF PERKINELMER XRD 1611	22
TABLE 3. SIGNAL-TO-NOISE RATIO FOR IMAGES IN FIGURE 17.	33
TABLE 4. PSEUDOCODE FOR RESIDUAL-WEIGHTED TOTAL VARIATION MINIMIZING POCS ALGORITHM	34
TABLE 5. IMAGE CHARACTERISTICS FOR FIGURE 23	44
TABLE 6. IMAGE CHARACTERISTICS FOR FIGURE 24	44

## LIST OF FIGURES

FIGURE 1. CONTRIBUTION TO AVERAGE EFFECTIVE DOSE TO US POPULATION, 2007	2
FIGURE 2. MASS ATTENUATION COEFFICIENTS FOR VARIOUS TISSUES AND MATERIALS	6
FIGURE 3. INTERACTION CROSS-SECTIONS FOR BARIUM AND WATER	7
FIGURE 4. X-RAY CT ACQUISITION SYSTEM	9
FIGURE 5. SYSTEM MATRIX ILLUSTRATION	10
FIGURE 6. SINGLE ROW OF SINOGRAM FOR A GREEN PEPPER	12
FIGURE 7. CONSTRUCTION OF ENTIRE SINOGRAM	13
FIGURE 8. BACKPROJECTION OF COLLECTED LINE INTEGRALS	15
FIGURE 9. BACKPROJECTION OF SHEPP-LOGAN HEAD PHANTOM	16
FIGURE 10. SIMPLE ART ALGORITHM FOR 3X3 GRID	19
FIGURE 11. ILLUSTRATION OF GEOMETRIC PENUMBRA EFFECT	23
FIGURE 12. SIDE VIEW OF X-RAY CT SYSTEM (PARALLEL TO Y AXIS)	25
FIGURE 13. SOURCE-IMAGER GEOMETRY FOR DETERMINATION OF SID.	26
FIGURE 14. GRADIENT-BASED PROJECTION OFFSET METHOD	27
FIGURE 15. SIDE- AND TOP-DOWN VIEWS OF SYSTEM AND ASSOCIATED GEOMETRY	29
FIGURE 16. FIRST PLANAR IMAGES FROM SYSTEM	30
FIGURE 17. FBP VS ART FOR A GREEN PEPPER, VARYING VIEWS	32
FIGURE 18. REWINDOWED 360-VIEW ART IMAGE SHOWING CORNER ERROR	35
FIGURE 19. POSITIVE-CONSTRAINED TSVD IMAGE OF A PEPPER SLICE	36
FIGURE 20. EFFECT OF FILTRATION ON TSVD RECONSTRUCTION OF PEPPER.	37
FIGURE 21. UNREGULARIZED VS. TIKHONOV-REGULARIZED IMAGES OBTAINED BY ICG	39
FIGURE 22. UNREGULARIZED VS. TV-REGULARIZED IMAGES OBTAINED BY ART	41
FIGURE 23. COMPARISON OF ALGORITHMS FOR PEPPER DATASET	42
FIGURE 24. COMPARISON OF ALGORITHMS FOR PEACH DATASET	43

## LIST OF ABBREVIATIONS

ALARA	AS LOW AS REASONABLY ACHIEVABLE
ART	ALGEBRAIC RECONSTRUCTION TECHNIQUE
CT	COMPUTED TOMOGRAPHY
FBP	FILTERED BACKPROJECTION
ICG	ITERATIVE CONJUGATE GRADIENTS
KVP	KILOVOLTAGE PEAK
LSF	LINE SPREAD FUNCTION
POCS	PROJECTION ONTO CONVEX SETS
PSF	POINT SPREAD FUNCTION
ROI	REGION OF INTEREST
RWTV-POCS	RESIDUAL WEIGHTED TOTAL VARIATION – PROJECTION ONTO CONVEX SETS
SAD	SOURCE-TO-AXIS DISTANCE
SID	SOURCE-TO-IMAGER DISTANCE
SNR	SIGNAL-TO-NOISE RATIO
SVD	SINGULAR VALUE DECOMPOSITION
TSVD	TRUNCATED SINGULAR VALUE DECOMPOSITION
TV	TOTAL VARIATION

# Chapter 1 – Introduction

---

## 1.1 Importance of x-ray imaging in medical practice

Since the discovery of x-rays by Röntgen in 1895, x-ray technology has played a pivotal role in the development of medical imaging. In diagnostic practice, plane radiographs have historically been used when high-contrast skeletal images were required. Due to the development of computed tomography (CT) by Hounsfield and Cormack, x-ray CT offers a number of advantages over plane radiography, including distinction of tissues on the basis of electron density, distinction of plane-superposed structures, and reformatting of volumetric images into different anatomical planar views.

It is hard to understate the importance of CT imaging in modern medicine. As of 2009, the number of CT scans performed in the United States had increased by three times since 1993, to about 70 million annual scans (1). CT or MRI imaging were ordered in 15% of patients presenting with injuries in emergency rooms in 2007, increasing from only 6% in 1998 (2). In the 1980's, medical procedures contributed only 15% to the average effective dose to the US population. Comparing this dose to the average effective dose to US population in 2006 (figure below), there is a dramatic increase in the percentage of dose due to medical procedures: about 50% of all medical dose in 2007 was due to CT scans (3).



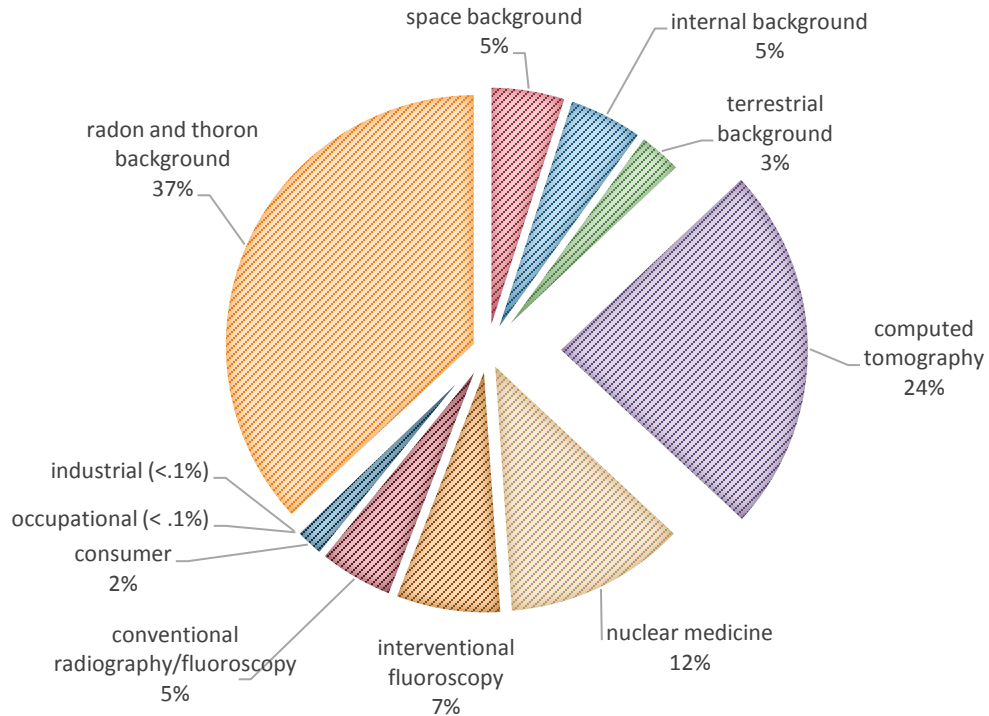


Figure 1. Contribution to average effective dose to US population, 2007. From (3).

CT scans are relevant not only to diagnostic medical practice, but also to therapeutic radiation delivery. Cone-beam computed tomography (CBCT) is an increasingly utilized imaging modality, particularly in radiation oncology. On-board imaging systems, such as those included on linear accelerators developed by Varian Medical Systems, allow for precise verification of patient positioning during the course of radiotherapy. This technique is referred to as image-guided radiation therapy (IGRT), and often employs on-board CT. A widely used algorithm for reconstruction of a three-dimensional dataset from two-dimensional cone-beam projections was developed by Feldkamp, Davis, and Kress (4), as an extension of filtered backprojection reconstruction (FBP), discussed in detail later.

There is, of course, a tradeoff between radiation dose and quality of image in x-ray imaging. Contrast-to-noise ratio as well as signal-to-noise ratio decrease with the number of photons

reaching the detector. With the number of photons and good signal characteristics of an image come imaging dose – an unavoidable side effect of photon interactions with matter. There is an increasing amount of concern over amount of imaging dose from routine and diagnostic medical procedures (5). Excess relative cancer risk is frequently quoted as being between 5% and 6% per Sievert (6) (7). Patient dose should be kept as low as reasonably achievable (ALARA), in order to minimize these risks.

As an illustrative example from de Gonzalez et al (1), the number of CT scans conducted in the US in 2007 has been estimated at 72 million, with 57 million of these performed not in the last five years of life or attributable to a cancer diagnosis. With an average of 10 *mSv* per scan and excess relative risk of 5% per Sievert, the scans in 2007 might have induced a crop of up to about 29,000 cancers. With an estimate of 50% mortality, the authors guess that this corresponded to a total of 14,500 deaths due to CT scans alone – a mortality rate of roughly one in 4,000. Excess relative risk of cancer is dependent on several factors including the age at which a patient is exposed to radiation and patient sex. The authors of (8) estimated that the risk of cancer is as high as 1 cancer in 270 exposures for 40-year-old women receiving CTs for coronary angiography.

Reduction of patient dose may in many cases be unachievable – diagnosis of certain conditions will necessarily require the higher contrast that is only afforded by CT imaging. In many cases, the only way to reduce dose will be to either not perform an imaging study at all or to reduce the amount of dose delivered during the study.

Fortunately for the patient undergoing the scan, there is much work being done to ameliorate concerns over imaging dose. One of the most prominent approaches for reduction of imaging dose is to simply reduce the number of views taken about the object, a technique termed “sparse-

data” or simply “sparse” tomography (9), with a wide range of techniques (10) (11) (12) (13) (14) (15) employed to accomplish the reconstruction. Unfortunately, implementation of new and improved algorithms which may lead to dose reduction has historically been slow, due to multivariate factors (16).

## 1.2 Objectives

One of the primary goals of this work is to implement a fully-functional CT reconstruction system, using available components. The system should be capable of fan-beam reconstruction, and MATLAB codes developed for parsing of detector datasets and reconstruction of imaged volumes. System geometry should be designed such that a range of objects may be imaged in industrial-like acquisition while maintaining good quality of reconstructions.

The other primary goal of this work is to demonstrate a few methods for sparse-data x-ray CT regularization – namely, Tikhonov regularization and total variation (TV) regularization through iterative reconstruction modalities. One specific method, total variation regularization via projection onto convex sets, outlined by Sidky, Kao, and Pan in (17), has shown good results on test datasets including the Shepp-Logan head phantom (18). It has been updated (19) and shown to be noise-robust via an adaptive-weighting technique (13). A modification to the algorithm in (17) is presented, and reconstructions from this modification are compared against standard algebraic reconstruction, FBP, and Tikhonov-regularized results.

## Chapter 2 – Background

---

### 2.1 Principles of x-ray CT imaging and reconstruction

The fundamental problem in x-ray CT reconstruction lies in recovering the distribution of the linear attenuation coefficient  $\mu$  for an object from a measured set of line integrals obtained from transmitting x-rays through the object. According to the Beer-Lambert law governing attenuation of photons,

$$I = I_0 * e^{-\mu x}, \quad (1)$$

where  $I$  the intensity of the beam as it exits the object,  $I_0$  is the incident intensity,  $\mu$  is the linear attenuation coefficient, and  $x$  is the thickness of the object.

The attenuation coefficient is usually expressed in  $cm^{-1}$  or  $mm^{-1}$ , and is an expression of the probability of removal of a photon from the incident beam per unit of distance traveled inside the material. Of the three primary interactions by which photons interact with matter – pair production, Compton scatter, and the photoelectric effect, those most important in energy regimes typical to diagnostic imaging are Compton scattering and the photoelectric effect. Typically,  $\mu$  is expressed as a *mass attenuation coefficient*,  $\mu/\rho$ , in units of  $cm^2/g$ , from sources such as NIST (20) in the US. Thus, the distribution of  $\mu$  recovered in CT imaging is a product of the mass attenuation coefficient and the material density. Because  $\mu$  is a function of density, material distinction from reconstructed images is often a difficult to impossible task without recourse to other methods such as dual-energy or spectral CT (21).

Narrowing the energy window on the x-ray source provides some recourse, as does knowledge of the subject of the imaging study (i.e. usually a human patient). In the diagnostic

energy range (that is, 20~150 *keV*), mass attenuation coefficients are very close for a range of organic materials and elements which compose human tissue (see Figure 2), especially as voltage increases. Due to this effect, it may be said that  $\mu$  is nearly proportional to density  $\rho$ , and with scaling, a recovered map is roughly a density map. This is a progressively worse approximation in lower energy regions for materials with k-edge absorption effects, including common contrast agents such as barium and iodine. Interaction cross sections for photoelectric and Compton scatter are shown for barium and water in Figure 3.

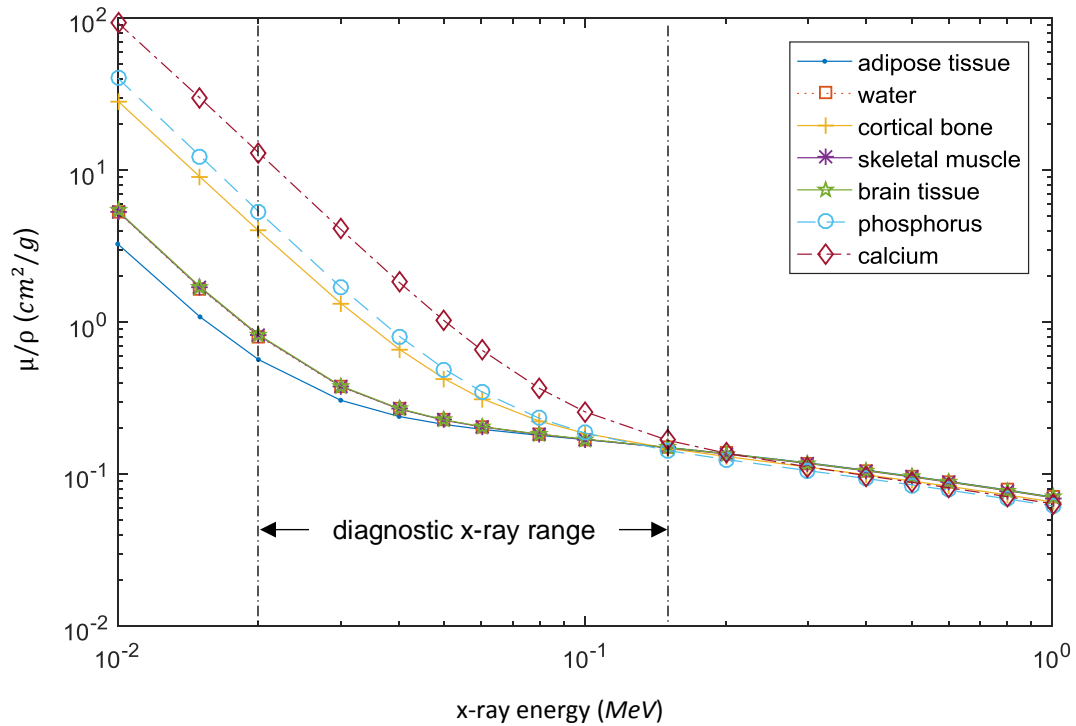


Figure 2. Mass attenuation coefficients for various tissues and materials. Data from (19).

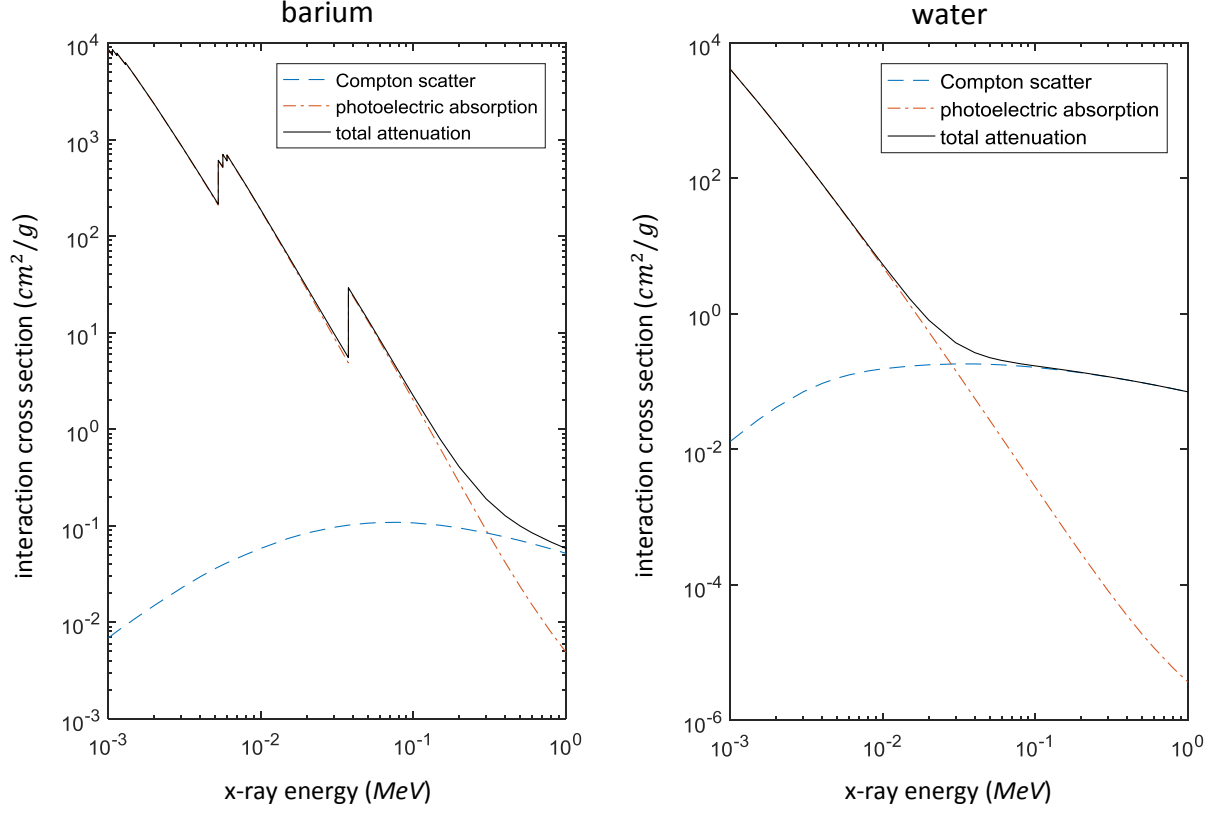


Figure 3. Interaction cross-sections for barium and water (19)

The form of the Beer-Lambert law in Equation (1) is only relevant for objects of uniform composition, and therefore uniform  $\mu$ . A more relevant expression which accounts for inhomogeneities of composition is:

$$I = I_0 * e^{-\int \mu dx},$$

$$\therefore \frac{I}{I_0} = e^{-\int \mu dx}, \quad (2)$$

where  $\mu$  varies in  $x$ .

For the problem to be computable, the image must take on a finite element form (consisting of pixels or voxels, in the three-dimensional case), as a reconstruction of the

attenuation coefficient distribution with arbitrary precision would require arbitrary physical storage. The integral in equation (2) is replaced by a summation of the products  $\mu_i x_i$  – that is, any ray crossing the volume of interest traverses through  $i$  pixels, each with attenuation coefficient  $\mu_i$  and an associated ray path length in pixel  $i$  of  $x_i$ .

$$\frac{I}{I_0} = e^{-\sum_i \mu_i x_i} \quad (3)$$

Following from this, it is readily evident that

$$-\log\left(\frac{I}{I_0}\right) = \sum_i \mu_i x_i \quad (4)$$

where the function  $\log()$  represents the natural logarithm. From this expression, the problem of CT reconstruction is clear – the distribution of the attenuation coefficients  $\mu_i$  is to be recovered from the measured intensity  $I_0$  at the detector and the incident intensity  $I$ . In order to recover information concerning the  $\mu$  distribution, the set of ray path lengths through pixels in the volume of interest  $x_i$  is also necessary.

Figure 4 shows a typical CT system, where the source and detector are situated along a line of response and the rays from the source pass through the volume to the detector. In this type of acquisition, the trajectories of the source and detector cover linear distance about the circumference of the FOV – a “patient”-type acquisition, ubiquitously employed by commercial medical scanners. Via a coordinate transform, however, the same geometry may be replicated by rotation of the imaged object on a stage while the source and imager remain stationary – an “industrial”-type acquisition, used, e.g., for nondestructive assays of manufactured parts and microtomography, where the system’s spatial resolution is on the order of microns. A system

with industrial-like acquisition characteristics is designed in this work, though as stated the two schemes function analogously to one another.

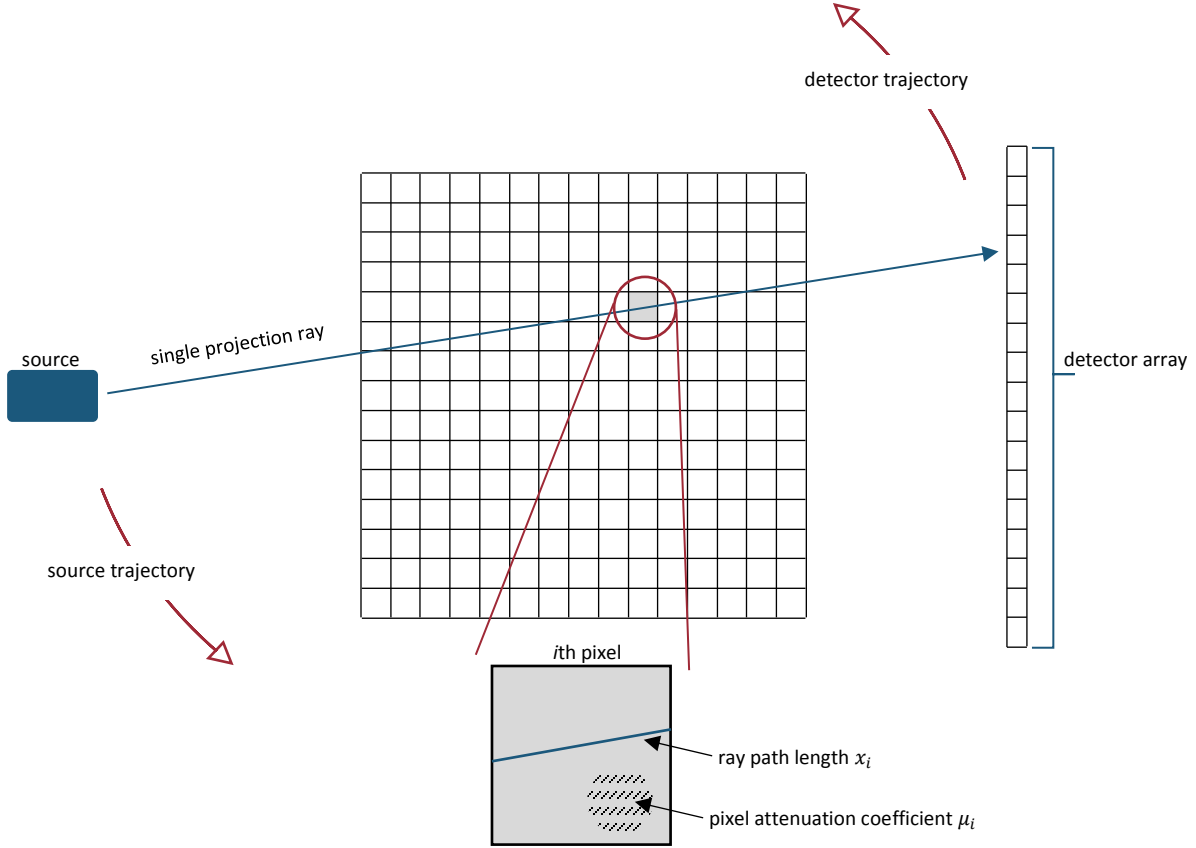


Figure 4. X-ray CT acquisition system

The ray-crossing path length coefficients  $x_i$  must be tabulated for each individual ray traversing from source to each detector. As the source and detector rotate about their respective trajectories (or as the object itself is rotated),  $p$  projections are taken of the ROI. Each of the  $r$  rays in each of the  $p$  projections has a crossing distance for each of the  $i$  pixels in the image – though for the majority of the pixels in the image, the crossing distance is 0 for any given ray. If



the source-to-imager distance is large enough in fan-beam geometries with respect to the source-to-axis distance, some rays may not cross the ROI at all.

The ray path length coefficients typically take the form of a *system matrix*, denoted by  $A$ . This matrix is effectively a full description of the geometry under which a set of data are acquired, and is directly applicable to the inverse problem of image reconstruction. It consists of the ray path lengths in all pixels corresponding to all rays in all projections – that is,  $x$  now carries three indices, for projection, ray, and pixel, as shown in Figure 5.

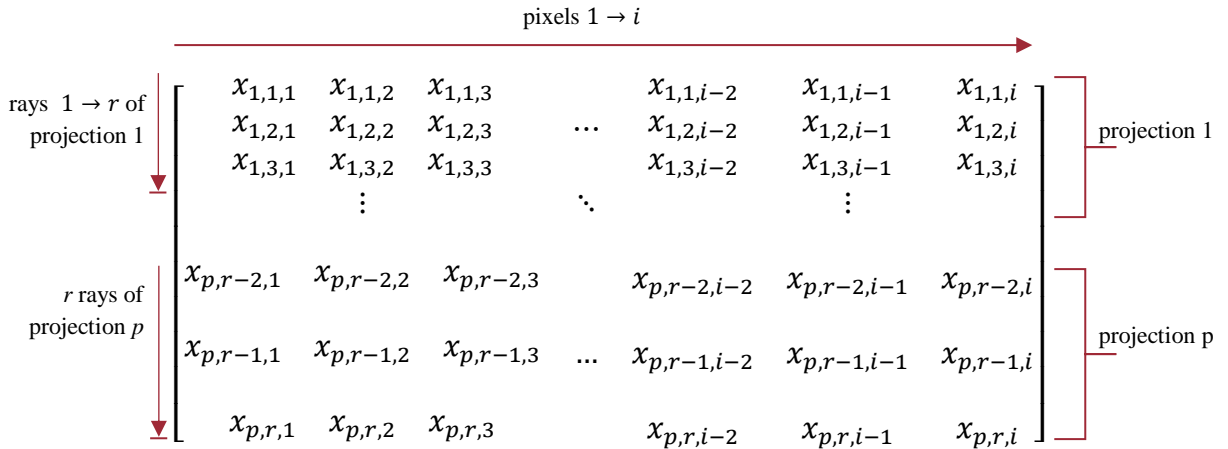


Figure 5. System matrix illustration

$A$  is typically a very large matrix. For the purpose of this work, an imaged array of 256 pixels on a side is considered, with 360 projections each involving 1024 detectors – that is, detectors are binned  $4 \times 4$  and photon counts are summed. A system matrix associated with this acquisition scheme contains  $\sim 24.2 \times 10^9$  elements, and if stored with 16-bit precision comprises 48.3 gigabytes of physical memory. Fortunately, it is also highly sparse, as most elements are

zero – with the source geometry used here (see Figure 15), the density of the sparse matrix  $A$  is only 0.12%. Reduction of strain on computational resources is thus possible via storage as a sparse data structure.

Calculation of the system matrix elements in  $A$  is a nontrivial matter – one commonly used algorithm for generation of  $A$  is Siddon’s ray-tracing method (22). Instead of treating pixels or voxels directly, this method treats image elements as intersection areas of a constructed set of parallel parametric planes which are mutually orthogonal. A parametric index  $\alpha$  is determined for the intersection of a given ray with the planes, and evaluation of the parametric function of the ray at tabulated values of  $\alpha$  gives the coordinates of intersections. The  $\ell^2$ -norm of the difference between successive intersection coordinates yields the desired path-lengths, and the norms are pixel-associated via determination of the midpoints of the intervening line segments.

A data structure containing the (linearized) measured intensity ratios,  $m$ , must also be incorporated into a reconstruction modality. This structure is called the *sinogram*, and is determinable from the measured intensities  $I$  for the detector channels at the imaging plane. By taking a bright field image before data acquisition, a baseline maximum intensity can be measured for  $I_0$ . The intensity ratio may be calculated directly and linearized.

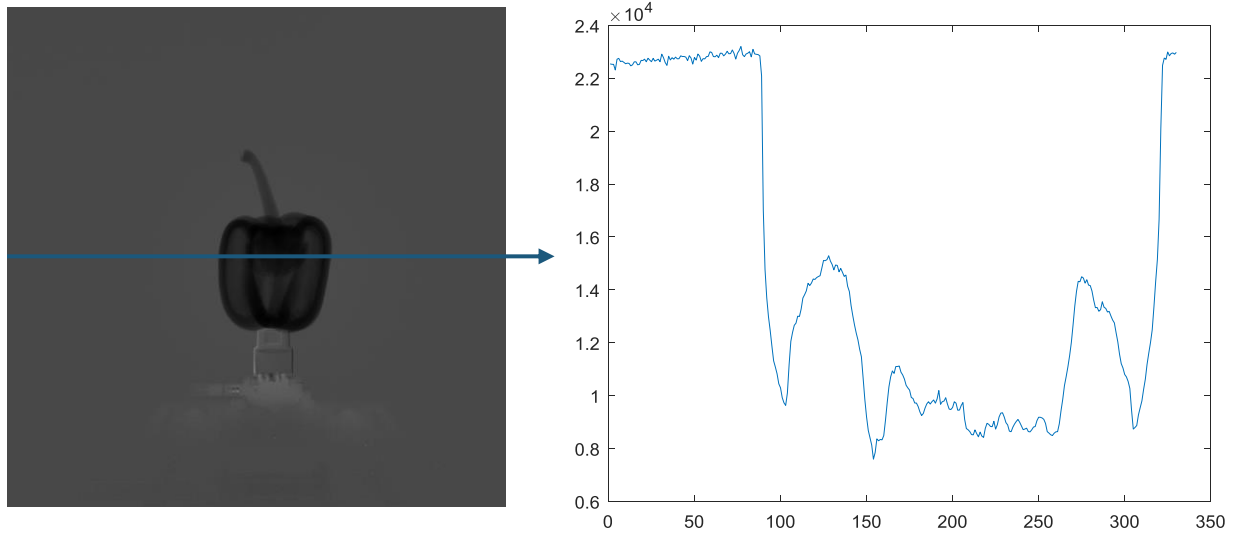


Figure 6. Single row of sinogram for a green pepper. Left: single two-dimensional projection from first projection angle, with horizontal centerline highlighted. Display window [min max]. Right: Signal level from highlighted detector channels, truncated to center 330 channels. Maximum detector signal: 65535.

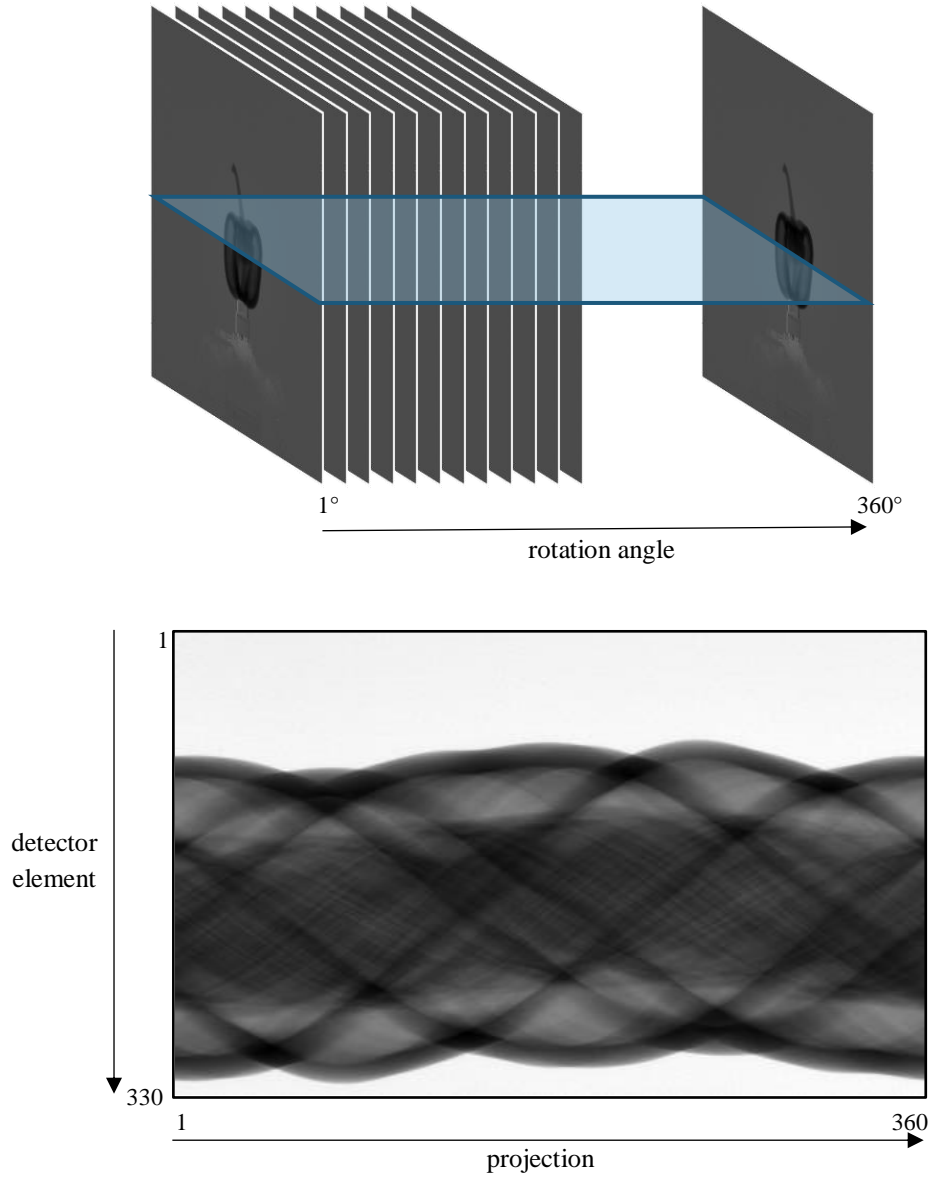


Figure 7. Construction of entire sinogram. Top: Successive two-dimensional projections are taken as object rotates – for simplicity, one projection is shown per rotational degree. Display window [min max]. Bottom: Signals from centerline detector channels as in Figure 6 are used from each of the rotational projection views to construct the sinogram. Display window [min max].

Figure 6 and Figure 7 above show how a sinogram may be constructed from a set of two-dimensional projections of an object. In construction of the sinogram, the data is transformed from an image  $f(x, y)$  into a set of line integrals characterized by radial distance from the origin and angular displacement from center of rotation, or  $p(r, \phi)$ .

To reconstruct an image, the task is then to recover the image data in  $f$ , where elements of  $f$  represent the attenuation coefficients – or roughly speaking, material density – of each pixel in the image. The relevant equation to be solved is

$$m = Af . \quad (5)$$

Computed tomographic reconstruction is therefore an *inverse problem* – a problem in which the factors producing a given result are recovered from the observations to which they have led. The problem is (ostensibly) linear as well, where the measurement obtained depends on a linear transform of the image. In practice, the assumption of linearity fails, due to noise on the measured data.

## 2.2 Reconstruction algorithms

X-ray tomographic reconstruction is a well-studied problem. Some of the very earliest work in inverse problems was pioneered by Ambartsumian (23), and Hadamard introduced the concept of *posedness*, where a well-posed problem is defined by three conditions: 1) that the solution exists, 2) that it is unique, and 3) that its behavior is continuous with respect to the input (24). The inverse of the Radon transform (25), the integral transform which generates a sinogram in two dimensions, is an example of an ill-posed problem. Condition 1 is usually met for x-ray tomography – the solution is the image to be recovered. Uniqueness is a more difficult condition to meet, as line integrals generated by rays crossing an image volume may take on the same values as those traversing the same volume without noise. It is readily evident that condition 3 is difficult to impossible to meet for x-ray tomography as well, when considering the methodologies used to recover image data.

### 2.2.1 Filtered backprojection

Backprojection refers to the process by which the path length-weighted linearized sinogram values are used to reconstruct an image. With appropriate projection normalization, this is a simple way to reconstruct an image from its line integrals. It is the most commonly employed analytical inverse of the Radon transform.

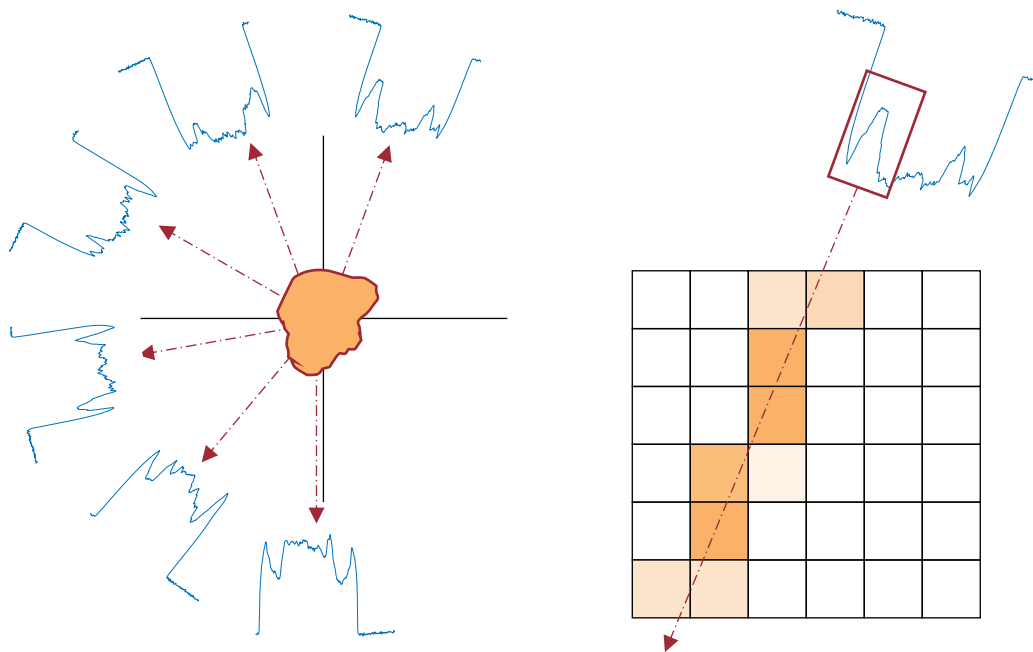


Figure 8. Backprojection of collected line integrals. Left: Line integral sets collected about many rotational angles. Right: Backprojection of a single signal peak along its ray path.

Direct backprojection yields images with blurring and lowered contrast, as shown in Figure 9. This phenomenon can be explained via Fourier analysis – Bracewell’s central slice theorem (26) states that the lines of a two-dimensional Fourier transform of an image  $f(x, y)$  may be filled by the one-dimensional Fourier transforms of the parallel projections of that object. That is,

$$f(x, y) = \mathcal{F}^{-1}\{F(k_x, k_y)\}, \quad (6)$$

where the Fourier-domain image  $F$  is filled by the one-dimensional transforms

$$P(k_r, \phi) = \mathcal{F}\{p(r, \phi)\}. \quad (7)$$

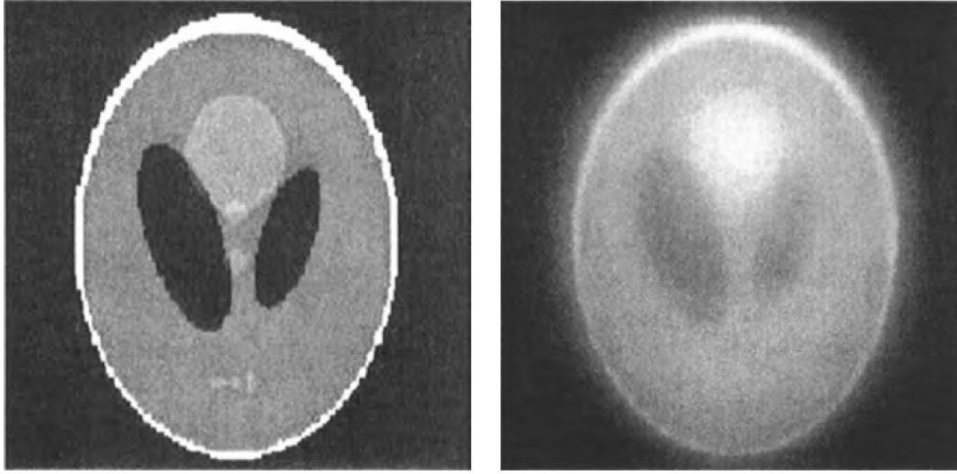


Figure 9. Backprojection of Shepp-Logan head phantom. Left: ground-truth image of phantom. Right: Image obtained by backprojection shows contrast loss and blurring. From ref (41).

In the frequency domain, the reason for appearance of artifacts on the reconstructed image  $f$  is apparent – sampling frequency is nonuniform, with oversampling near the image center, and undersampling increasing with radial displacement from the center. A common solution to this problem is to apply a filter weighting the amplitude of the frequency-domain signal by the radial sampling frequency  $k_r$ . The simplest of these is the ramp filter,  $H(k) = |k|$ . Other popular filters include the Hanning filter (27) and the Hamming filter (28). Frequency-domain filtering gives rise to the name “filtered backprojection.”

Frequency-domain analysis also gives minimal sampling criteria for filtered backprojection – source trajectories with small-angle coverage will not fill the image’s Fourier transform. For parallel-beam geometries, at least  $180^\circ$  of beam coverage is necessary. For fan-beam acquisition, the trajectory must cover at least  $180^\circ + \varphi$ , where  $\varphi$  represents the central fan beam angle.

Filtered backprojection is subject to constraints which make it unattractive when considering sparse-data reconstruction. Due to the nature of sampling of signal frequency, the Nyquist criterion must be met – that is,

$$\Delta r \leq \frac{1}{2k_{max}}, \quad (8)$$

where  $\Delta r$  is the angular sampling distance about the trajectory and  $k_{max}$  is the maximum frequency of the output signal. Ideally  $k_{max} = (\text{imager resolution})^{-1}$ , but in practice the actual maximum resolution is the full width of the output signal at half the maximum response – or, full-width half-max, FWHM, characterized by the point- or line-spread function (PSF or LSF) of the system. The line-spread function, for example, is the FWHM of the detector’s response function to a one-dimensional linelike object. The imaging spatial resolution is affected by factors including detector-level electronic noise, photon scatter, and focal spot size.

Filtered backprojection and its variants, including the Feldkamp-Davis-Kress algorithm for cone-beam reconstruction (4), are widely studied (29) (30) (31) and have seen widespread use in commercial systems employed by hospitals for the last 30 years, despite major progress being made in the field of inverse problems (see: the journal simply titled *Inverse Problems* published by IOP). Pan et al suggest that a significant issue preventing implementation of novel algorithms is lack of communication between engineers working on CT and mathematicians (16). One of the goals of this work is to show that iterative and other techniques used for sparse-



data reconstruction (and toward lower overall medical dose) can be implemented even on consumer-grade hardware, thus helping to bridge the gap between the theory and application of inverse solution techniques.

### 2.2.2 Other analytical techniques

Because the problem in CT is to solve Equation 5 for  $f$ , it may seem that the simplest way to solve the system is to simply obtain the matrix inverse for the easy solution  $A^{-1}m$ . If the matrix  $A$  is invertible, the relative residual

$$\frac{\|m - A f_0\|_2}{\|m\|_2}, \quad (9)$$

where  $f_0$  is the obtained approximation to the image, will ostensibly be zero.  $A$  is typically not square and therefore not invertible, so the Hadamard conditions are not met. To find a unique solution analytically, the matrix pseudoinverse  $A^\dagger$  may be employed. The pseudoinverse may be constructed using the singular value decomposition (SVD),  $A = U D V^T$ . As  $A$  will ostensibly not be full-rank, a range of least-squares solutions exist, and the pseudoinverse gives the minimum-norm least-squares solution (32).

The pseudoinverse is usually far too large in practical imaging circumstances to store, and instead its components  $V$ ,  $D^\dagger$ , and  $U^T$  are applied piecewise to data. Further, the condition number of the matrix  $A$  is typically very large, implying high sensitivity of reconstructions to measured data perturbations. Real datasets used in tomography always contain perturbations as noise – one method for data regularization using the SVD is truncated singular value decomposition (TSVD), discussed in (32). Though the TSVD solution may fit the data well algebraically, it will likely also carry obvious errors due to amplification of data noise through the pseudo-inversion. A thorough discussion of linear algebra and matrix analysis is well beyond

the scope of this work, but TSVD is mentioned as illustrative of the tradeoff between a solution carrying low residual and being apparently “smooth” or well-regularized (see Results). Useful discussion can be found in (33), (34) and (35).

### 2.2.3 Iterative approaches

Iterative methods in linear system solutions are widely used – a method discovered by Kaczmarz (36) was later adapted to iterative reconstruction (37) by Gordon et al as an algebraic reconstruction technique (ART). ART shares with FBP that measured signals are back-projected into the image domain. While FBP backprojects all line integrals at once and remedies artifacts of nonuniform sampling frequency with a filter, ART schema employ intensive computation methods to update approximations to the image, which ideally converge to the actual image after a finite number of iterations.

An example of ART can be used in solving the following simple puzzle: given the sums of the rows and columns of a matrix, can the individual elements of the matrix be determined? As shown in Figure 10, this can be accomplished by weighted averaging of the sums, assignment of the averages to the “pixels,” and then adjustment of the approximations by weighted distribution of the row- or column-wise residual errors along the appropriate directions.

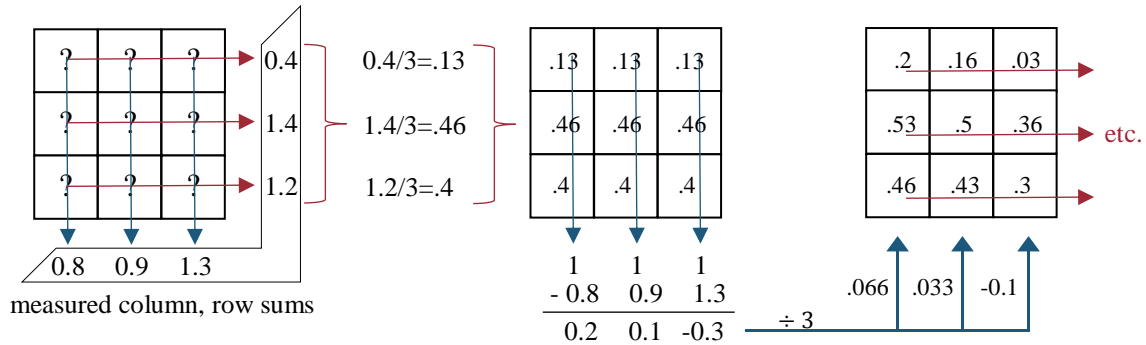


Figure 10. Simple ART algorithm for 3x3 grid

This leads intuitively to the expression

$$f_i^{k+1} = f_i^k - \ell * \left( (\mathcal{P}_{r,i}^k)^T * \frac{(\mathcal{P}_{r,i}^k - \mathcal{Q}_r^k)}{\sum_i (\mathcal{P}_{r,i}^k)^2} \right), \quad (10)$$

which is a statement of an ART algorithm similar to that used in the figure. Here  $f_i^k$  represents one iterative approximation to the image, where  $k$  is the iterator and  $i$  the number of pixels in the image,  $\mathcal{P}_{r,i}^k$  is the  $k$ th projection in the system matrix  $A$ , containing the ray-path intersection lengths for all  $r$  rays in one projection,  $\mathcal{Q}_r^k$  is the linearized projection data, and the superscript  $T$  denotes the matrix transpose as usual. The parameter  $\ell$  is a relaxation parameter dictating the weight of the update to the approximations.

Iterative reconstruction offers a few advantages over filtered backprojection. It is comparatively easier to incorporate prior knowledge concerning the output – as above in Equation 9, a solution will generally converge in fewer iteration loops if an appropriately chosen “guess” image  $f_i^0$  is provided. Iterative techniques are generally superior to FBP when considering sparsely sampled data, as the function of the matrix geometry is to appropriately assign weights to line profiles of varying intensity. It is comparatively easier to manage the projection model, and regularization can be incorporated into the iterative reconstruction process.

However, convergence is not guaranteed, and stopping criteria must often be chosen empirically, with noise as an important concern, as well as spatial resolution. Further, iterative techniques are usually incredibly taxing on physical computational resources, though much work is being done in GPU acceleration of these algorithms (38) (39) (40) (41), as well as in parallelization, exploiting the advent of affordable processors with multiple-core architecture (42).

## Chapter 3 – Design of x-ray ct system

---

### 3.1 Equipment and materials

Any system employing tomographic reconstruction of x-ray data will include, at minimum: an x-ray source or sources, detectors with associated electronics for determination of transmitted beam intensity, some positioning system capable of providing views of the imaged object from the several projection angles, and the nominal computed reconstruction system itself, with associated software and algorithms.

For this work, a 100 kV microfocus x-ray machine from Hamamatsu Photonics was the available source. Device specifications are shown in Table 1.

Table 1. Characteristics of Hamamatsu L9631 x-ray source

<b>maximum power output</b>	50 W
<b>voltage setting range</b>	40 to 110 kV
<b>current setting range</b>	10 to 800 $\mu A$
<b>focal spot size</b>	15 $\mu m$ (at 6W output) 80 $\mu m$ (at 50W output)
<b>x-ray emission angle</b>	62° maximum

The detector array used was a PerkinElmer XRD 1611 flat-panel photodiode array. This detector is attractive for a number of reasons, including sensitivity to high-energy x- and gamma rays, with possible application toward future work on reconstruction of integrity flaws in nuclear fuel rods. Characteristics for the XRD are shown in Table 2.

Table 2. Characteristics of PerkinElmer XRD 1611

<b>total pixel number</b>	<b>4096 x 4096</b>
<b>dot pitch</b>	100 $\mu m$ (no pixel binning) 200 $\mu m$ at 2x2 binning 400 $\mu m$ at 4x4 binning
<b>total active area</b>	409.6 mm x 409.6 mm
<b>dynamic range</b>	> 84 dB
<b>framerate</b>	3.75 fps nominal 7.5 fps at 2x2 binning 15 fps at 4x4 binning
<b>scintillator</b>	$Gd_2O_2S:Tb$ (gadox)
<b>sensitive radiation energy</b>	20 keV – 15 MeV

The detector's associated software contains tools for basic image processing and acquisition, but holds all projections for a dataset in memory at once. ROI selection is not supported, so full-datastream acquisition is necessitated. These factors and physical memory limit number of projections which may be included in a complete output dataset from the software.

### 3.2 Practical considerations of system design

#### 3.2.1 Focal spot penumbra effect

In imaging under a fan- or cone-beam geometry using an x-ray source with a nonzero focal spot size  $f$ , the resolving power is limited by the geometric unsharpness of the system (43). This effect is most readily apparent near the interfaces of piecewise-constant  $\mu$  distributions and object edges. It may appear as an outlying border to structures, where it is termed the geometric penumbra,  $P$ . Penumbra depends on  $SID$  and  $SAD$  as well as on focal spot size, as shown in Figure 11.

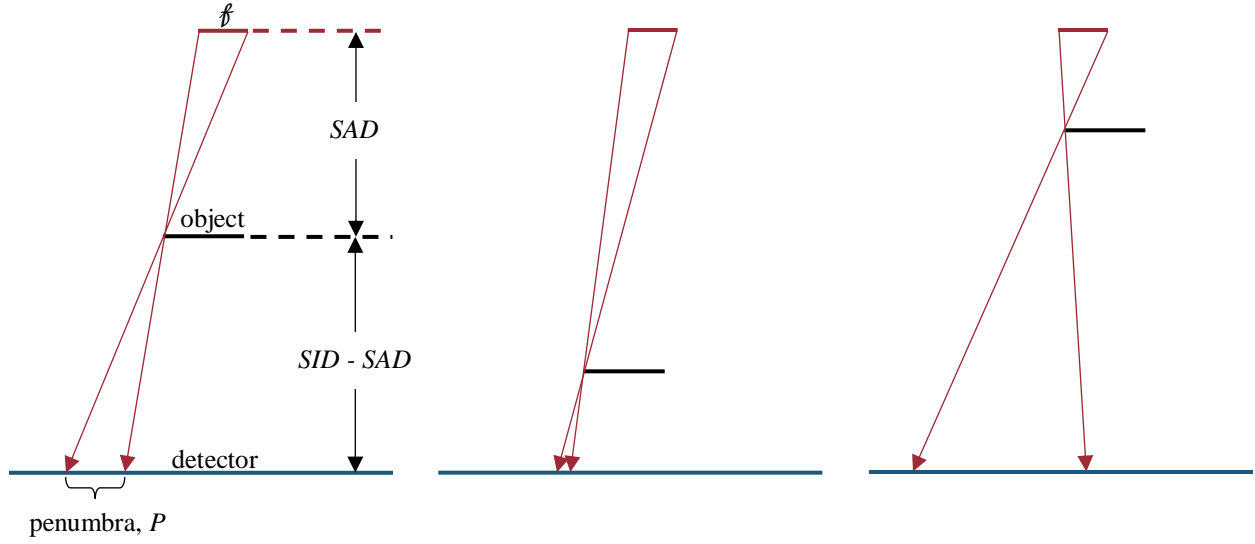


Figure 11. Illustration of geometric penumbra effect. Left: Source-to-axis and object-to-imager distances are nearly equivalent. Middle: Object close to detector, smaller penumbra. Right: Object close to source, larger penumbra.

By exploiting similar triangular geometries, it is apparent that

$$P = f * \frac{(SID - SAD)}{SAD}, \quad (11)$$

where  $f$ ,  $SID$ , and  $SAD$  are as defined above. Therefore, an imaged object should be situated as close as reasonably possible to the imaging plane, in order to decrease geometric penumbra and image blurring.

### 3.2.2 Signal-to-noise ratio

Signal-to-noise ratio (SNR) is a general metric for image quality, and is applied in computed tomography as well as in optical imaging, MRI, ultrasound, plane radiography, and nuclear medicine imaging. It is defined as

$$SNR = \frac{\bar{I}_{ROI}}{\sigma}, \quad (12)$$

where  $\bar{I}_{ROI}$  denotes the mean signal intensity in a given ROI in the image and  $\sigma$  the standard deviation of the image noise (43). The *SNR* of a reconstructed image scales with the square root of the number photons reaching individual detector elements – and therefore by kVp setting of the source (i.e. x-ray output energy), mA setting (i.e. areal intensity of radiation at detector), and exposure time.

Reconstruction schema affects SNR as well – one well-known example of reconstruction-associated noise is the “salt-and-pepper” noise pattern typical to algebraic reconstruction techniques (ART). Other factors contributing to SNR include detector efficiency, source-to-axis distance (i.e. beam intensity), and thickness of the reconstructed slice.

### 3.3 Measurement and construction

Design of source-stage-detector geometry proceeded as follows:

1. Create mounts for imaging plate and x-ray source, with horizontal imager centerline and source focal spot some height  $h$  along above optical table.

Vertical coordinate of radiation isocenter is limited by size of components – e.g., if stage height is significantly greater than focal spot height, no rays will pass through the imaging FOV. Horizontal centerline of imager and focal spot of x-ray source should be situated at identical vertical coordinate. This maintains ideal fan-beam geometry, avoiding introduction of an angular correction factor for the beam plane in reconstruction. Framing for imaging plate and source should also be designed and oriented such that mechanical isocenter (rotation stage), x-ray focal spot, and imager vertical centerline all have  $y = 0$ .

In practice, this would have been very difficult to accomplish. Mounting holes for x-ray source are  $M6 \times 1$  with 100 mm separation. Thorlabs optical table in use is based on United States

customary units and as such has mounting holes at 1-inch separation. One side of x-ray mounting base was fastened at two points, such that focal spot-to-mechanical isocenter separation is 0.8 mm.

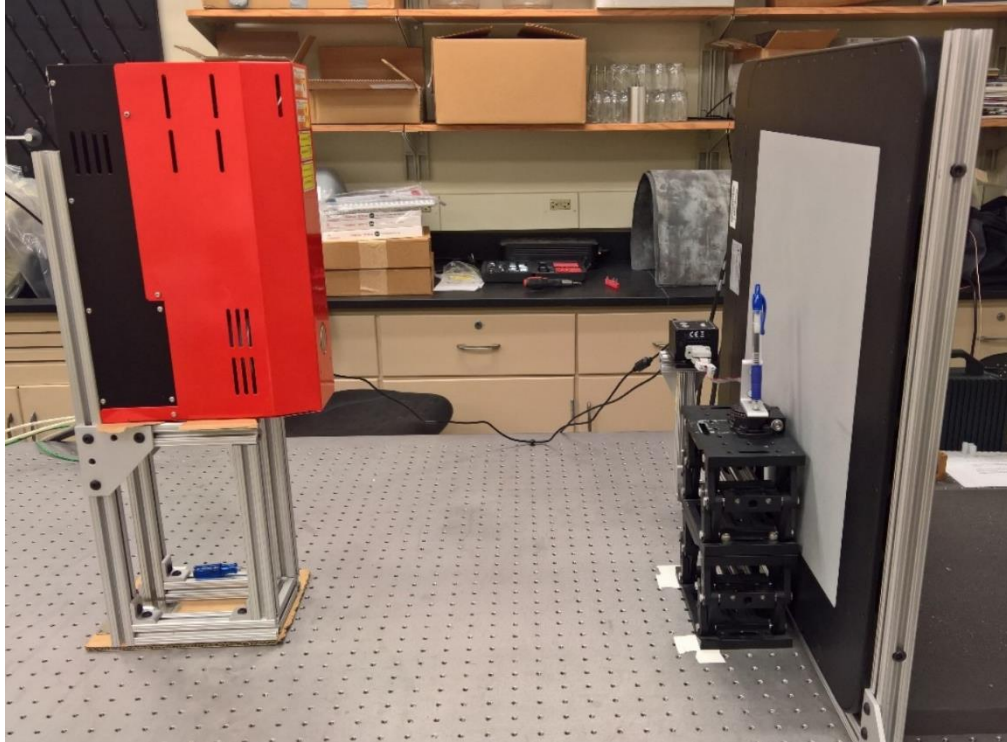


*Figure 12. Side view of x-ray CT system (parallel to y axis)*

2. Determine the minimum source-to-imager distance (SID), such that the x-ray cone homogeneously irradiates the entire active detector area.

For a cone beam with emission angle  $\theta$ , the minimum SID for homogeneous irradiation is a function of the radius  $r_d$  of the imaging array – the projected beam cone at the imager plane



should minimally circumscribe the entire active area (see Figure 13). For a square array of side  $s_d$ , it is evident that  $r_d = s_d\sqrt{2}$ , and that

$$SID \geq \frac{s_d\sqrt{2}}{2 \tan\left(\frac{\theta}{2}\right)}, \quad (13)$$

per Figure 13 below.

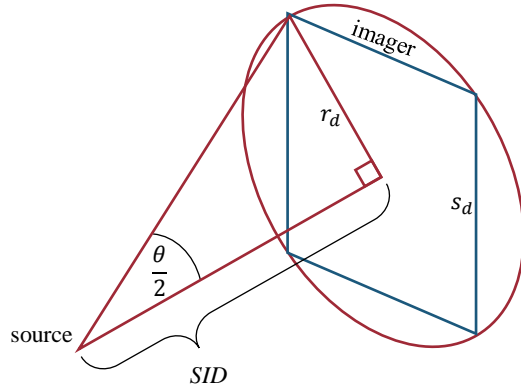


Figure 13. Source-imager geometry for determination of SID.

Homogeneous irradiation from minimal SID helps to keep SNR high, as described in (3.2.2).

3. Rotation stage was mounted on Thorlabs lab jacks, allowing height adjustment of imaged objects to imager channel centerline.

Jacks are situated between rails of 80/20 extruded aluminum, such that source-to-axis distance (SAD) is adjustable and a wider range of objects may be imaged while still maintaining acceptable signal-to-noise ratio and minimizing penumbra where possible.

4. Determine imager vertical centerline offset via projection.

This is a crucial step for software correction and ensures accuracy of matrices characterizing the system's geometry. Detector centerline could not be localized to y axis mechanically due to dimensional constraints. Projection coordinate determination was accomplished via a simple gradient-based method: objects were placed on rotation stage and a full 360° scan was acquired. The image gradient of the center-channel sinogram was determined, and summed along the projection indices. An iterative method was used to locate the channels corresponding to the first values exceeding half the maximum value of the aggregate gradient sum – the centerline between these channels was used to determine the offset. This method works well for a properly functioning detector and objects not sharply inhomogeneous, but fails if, for example, a metal-water equivalent interface is present, or if some detector channels are unresponsive.

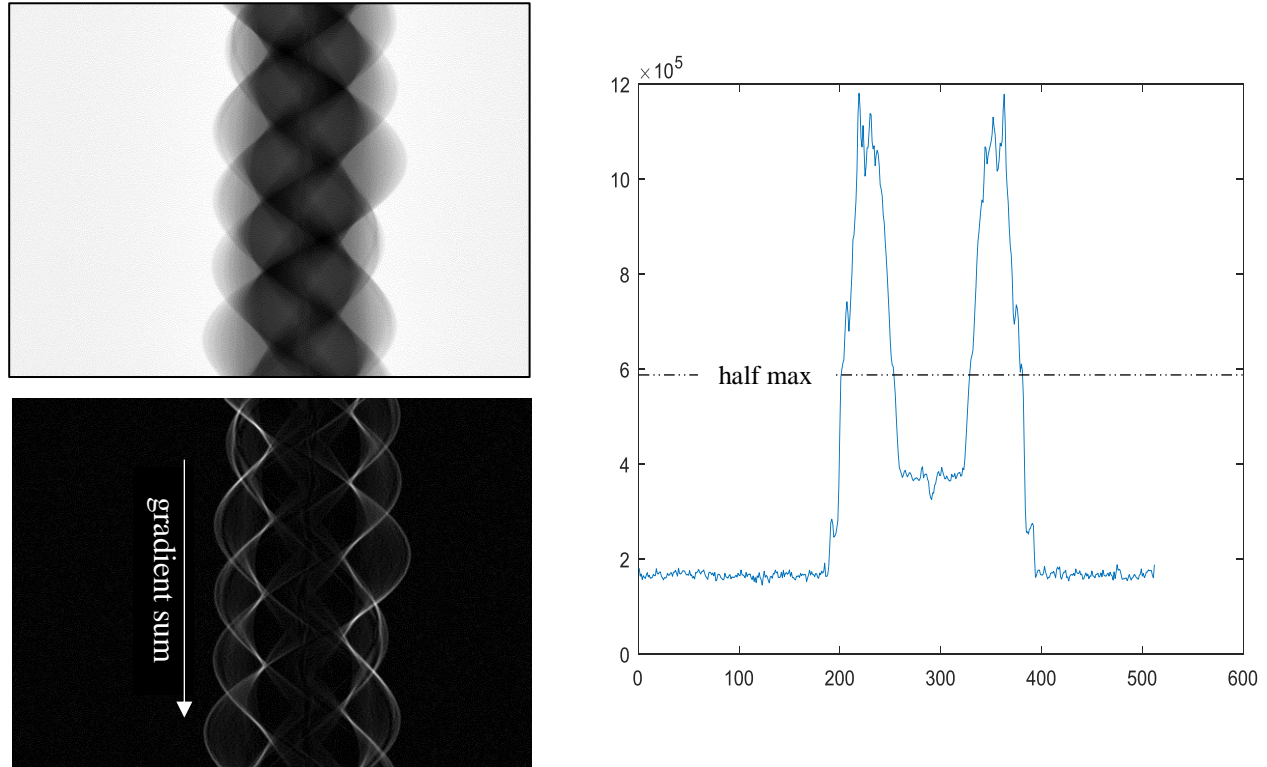


Figure 14. Gradient-based projection offset method. Top left: original sinogram. Bottom left: image gradient of sinogram, showing direction of summation. Right: Gradient sum

Reconstruction software used in this work was written in MATLAB r2014a and earlier versions. The filtered backprojection functions from Fessler and group (44) are used, which worked sans modification with the CT system. Functions created during this work include:

- `readxis`, which parses headers and contents of `.his` and `.xis` output files from the PerkinElmer XIS software to usable matrix data
- `sinobuild`, which constructs a sinogram from a set of two-dimensional projections taken at angular steps, with options for downsampling and truncation
- `fssc`, which corrects for the (very small) virtual-source displacement effect on SID and SAD
- `lart`, which implements in a straightforward manner the iterative step in Equation (10)
- `sof`, which returns the sinogram offset from the imager channel centerline, in detector units
- `weightmat`, which implements Siddon's ray tracing parametric method for construction of the system matrix  $A$ .

### 3.3.1 System geometry

Figure 15 below shows full geometric characteristics of the CT system. The imager's active area is square, and its dimensions are omitted as redundant in the side view, which principally serves to show the small horizontal offsets of component centers from one another.

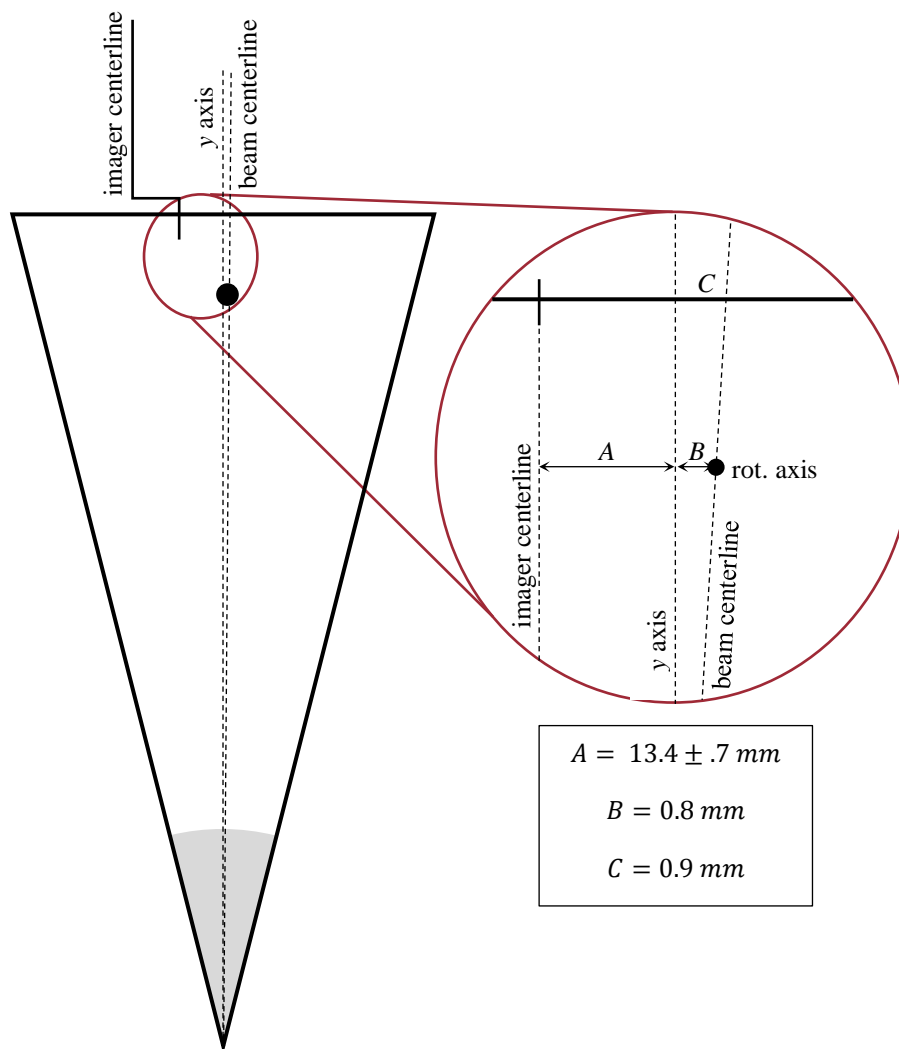
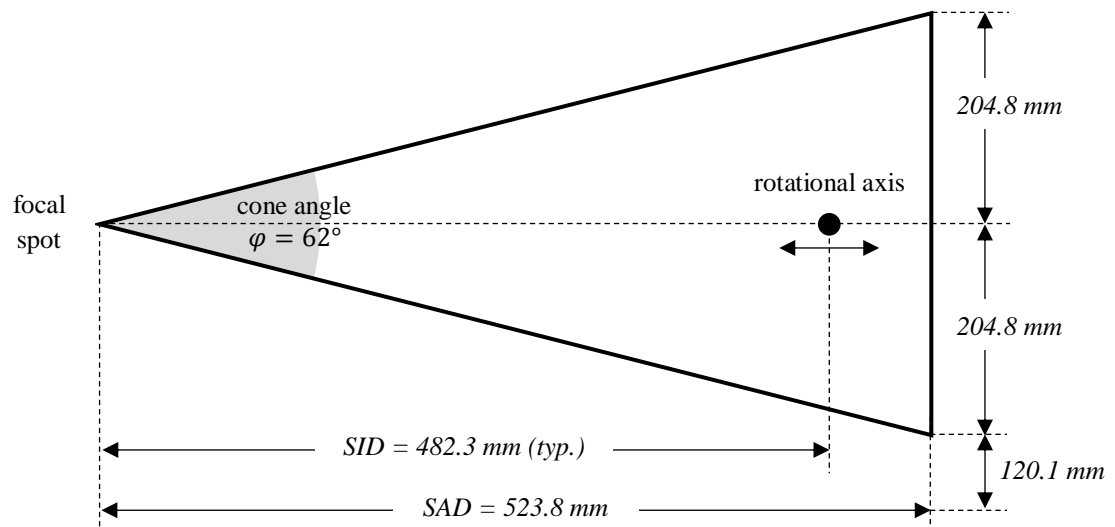


Figure 15. Side- and top-down views of system and associated geometry

## Chapter 4 – Results

---

Initial setup of the system was a lengthy process due to the need to machine parts for use in framing and mounting. The first planar images obtained on the new x-ray system prior to geometry finalization were of a bike pump and a set of keys. Initial reconstruction tests yielded generally poor results, until such factors as y axis offsets and sinogram offsets were determined precisely.

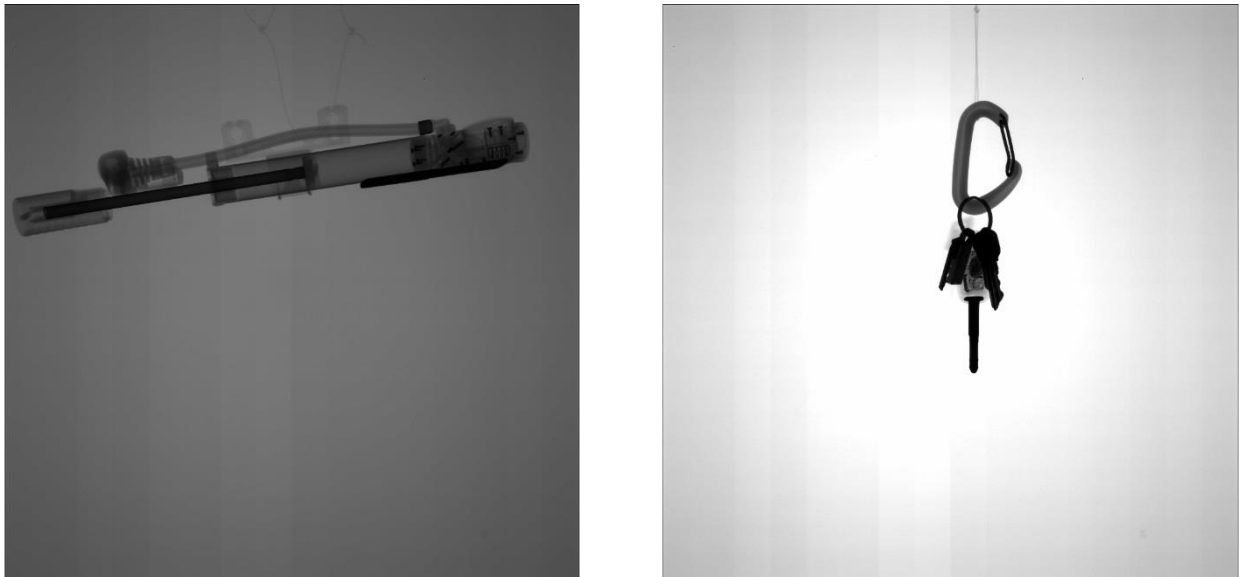


Figure 16. First planar images from system

### 4.1 Dataset acquisition

Several datasets have been acquired using this x-ray system, and are available for example exercises and illustration of reconstruction techniques via the MATLAB functions developed for this work or through other methods. Datasets acquired include a green *Capsicum* pepper, a peach, a starfruit (*carambola*), a solo papaya, a dragonfruit, and an apple.

All datasets were acquired with full-angular coverage scans, at one projection per angular degree of object rotation. Datasets for pepper, peach, and starfruit were acquired at the typical geometry as shown in Figure 15. Other datasets were acquired at nominal SAD minus one inch. All “sparsely sampled” data in this work is obtained via retrospective downsampling, and is sampled at uniformly spaced intervals about the object’s rotation.

#### *4.1.1 FBP and ART reconstructions*

Figure 17 shows the FBP- and ART- reconstructed images of a green pepper, using 360, 75, and 20 projections. Of particular note is the heavy aliasing from undersampling evident in the few-view FBP reconstructions. Table 3 shows the signal-to-noise ratio calculated for each of the images in Figure 17. ROI’s used for signal and noise calculation on all images are shown in figure.

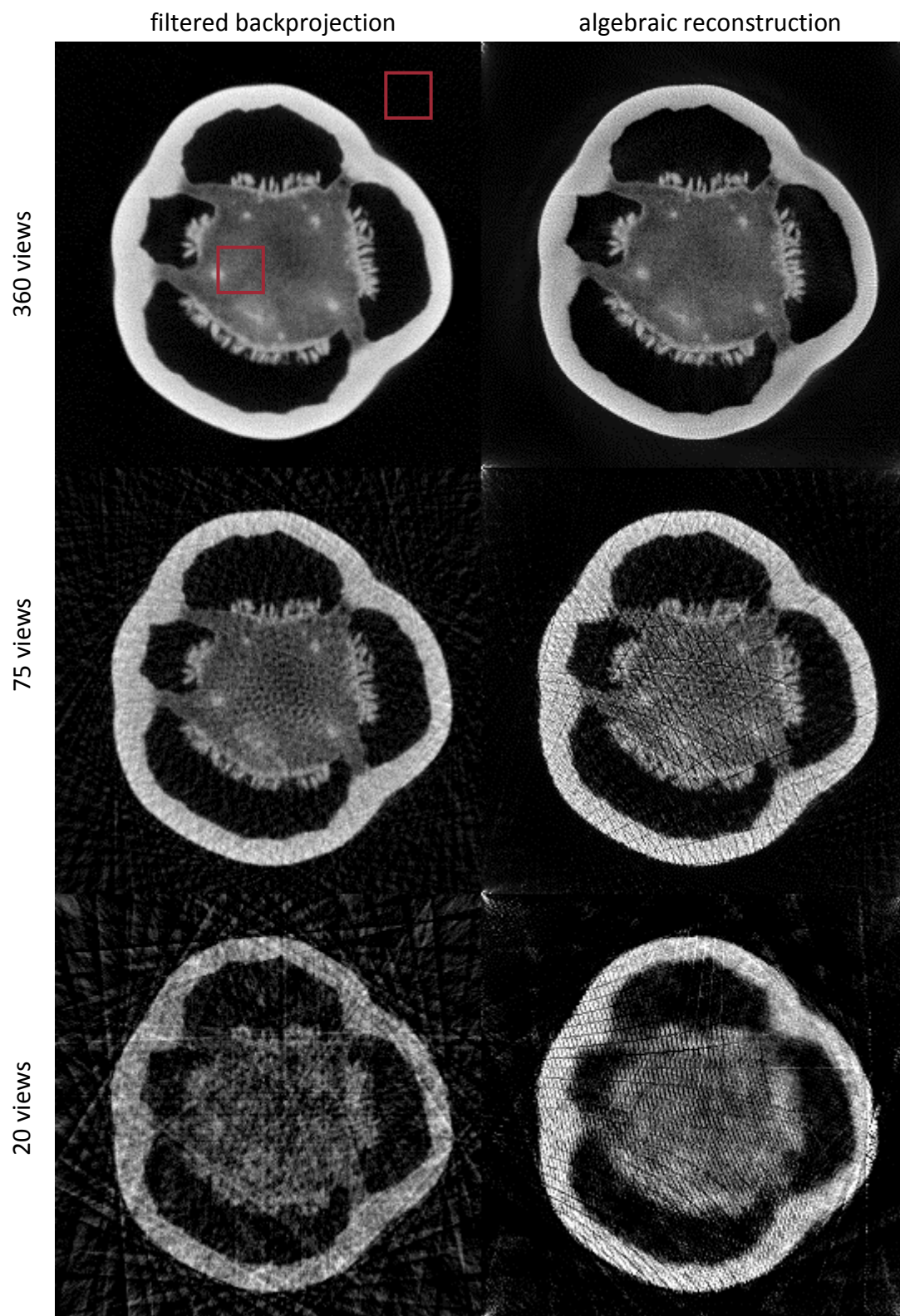


Figure 17. FBP vs ART for a green pepper, varying views. Display windows:  $[0 \ 0.325] \text{ mm}^{-1}$

Table 3. Signal-to-noise ratio for images in Figure 17.

	<b>FBP</b>	<b>ART</b>
<b>360 views</b>	14.52 dB	17.30 dB
<b>75 views</b>	8.01	12.22
<b>20 views</b>	3.92	12.03

The ART algorithm employed here is a modification of the simple update scheme seen in Equation 10. Specifically, residual weighting of projections is employed to construct the output image, with a loop-wise evaluation of fractional drift in residual as a stop criterion – instead of performing iterations through the entire set of data and then evaluating residual, the residual is constantly tracked with the updates to the image approximation. If the residual remains the lowest for a set number of iterations (i.e. the `hold` parameter), then the algorithm tabulates the residual-weighted sum image over the next complete set of views, and then normalizes this sum by the weights as the output image. The `while` loop (lines 5 – 29) in the following pseudocode is used in place of the usual `for` loop in the TV-POCS algorithm from (17), to create the residual-weighted total variation POCS (RWTV-POCS) method.

The TV-POCS algorithm is indicated to work well for images with largely sparse corresponding gradient images. It is expected that since the RWTV-POCS incorporates an extra loop to create an image following the gradient descent step in TV-POCS, that the RWTV variant will have typically lower residual, but higher total variation.



Table 4. Pseudocode for residual-weighted total variation minimizing POCS algorithm

1:	initialize $f = \text{uniform}(0)$ or $f = \text{input guess}$
2:	init $rres = \text{norm}(m - Af) / \text{norm}(f)$
3:	init $ticker = 0, n = 1, low = rres, viewnum$
4:	init $hold, restol$ [user defined]
5:	while ( $n < \text{maxiters}$ )
6:	update $f$ (see eqn 10)
7:	$f(f < 0) = 0$
8:	$rres = \text{norm}(m - Af) / \text{norm}(f)$
9:	if $0 \leq ticker < hold$
10:	if $rres < restol * low$
11:	$low = rres$
12:	$ticker = 0$
13:	elseif $rres \geq restol * low$
14:	$ticker = ticker + 1$
15:	end if
16:	else
17:	if $ticker == hold$
18:	$imgtally = f * (1/rres)$
19:	$rrtot = 1/rres$
20:	$ticker = -1$
21:	else
22:	$imgtally = tally + f * (1/rres)$
23:	$rrtot = rrtot + (1/rres)$
24:	end if
25:	end if
26:	if $ticker == -viewnum$
27:	break while
28:	end if
29:	end while
30:	$f = imgtally / rrtot$

This type of stopping criterion was chosen because solutions took a long time to converge (more than 10000 iterations) to small residuals, and often did not converge to a relative residual within 1% error. The parameters `hold` and `restol` are user-set for computing time, allowance of error, etc. Values used in this work are  $hold = \lceil 1.5 * viewnum \rceil$ , where  $\lceil \cdot \rceil$  represents the ceiling function, and  $restol = 0.995$ , unless otherwise specified.

Careful inspection of the edges and corners of the ART images reveals high signal levels at the periphery. This shunting of large error margins to the edges of the image is an undesirable

feature of ART. An image windowed to [min max] is shown in Figure 18, with a magnified corner. Regularization can be used to help smooth these regions of apparently large error.

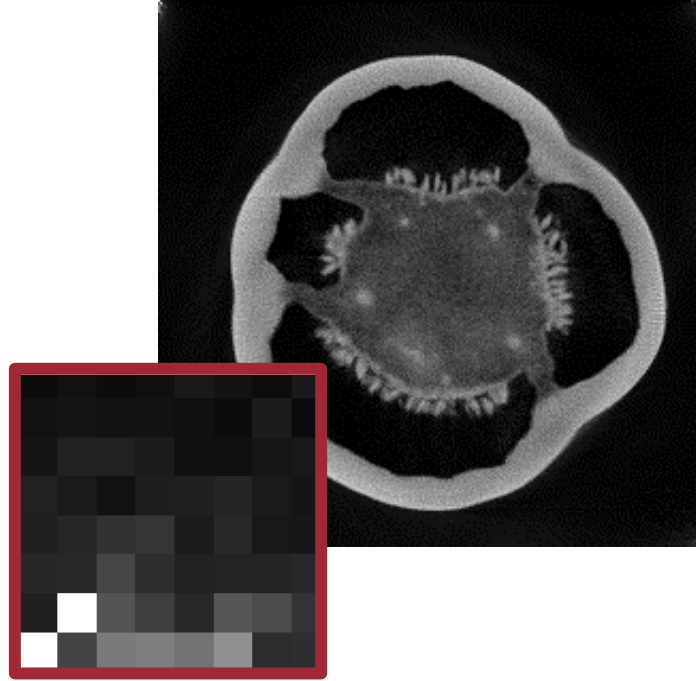


Figure 18. Rewindowed 360-view ART image showing corner error. Window [min max].

#### 4.1.2 TSVD method and characteristics

Figure 19 below shows a truncated singular value decomposition (TSVD) reconstruction, using the first 1000 singular values (due to memory constraints). The condition number  $d_1/d_{min}$ , where  $d_n$  are the  $n$  singular values cannot be exactly calculated from the truncated SVD, but is clearly large.

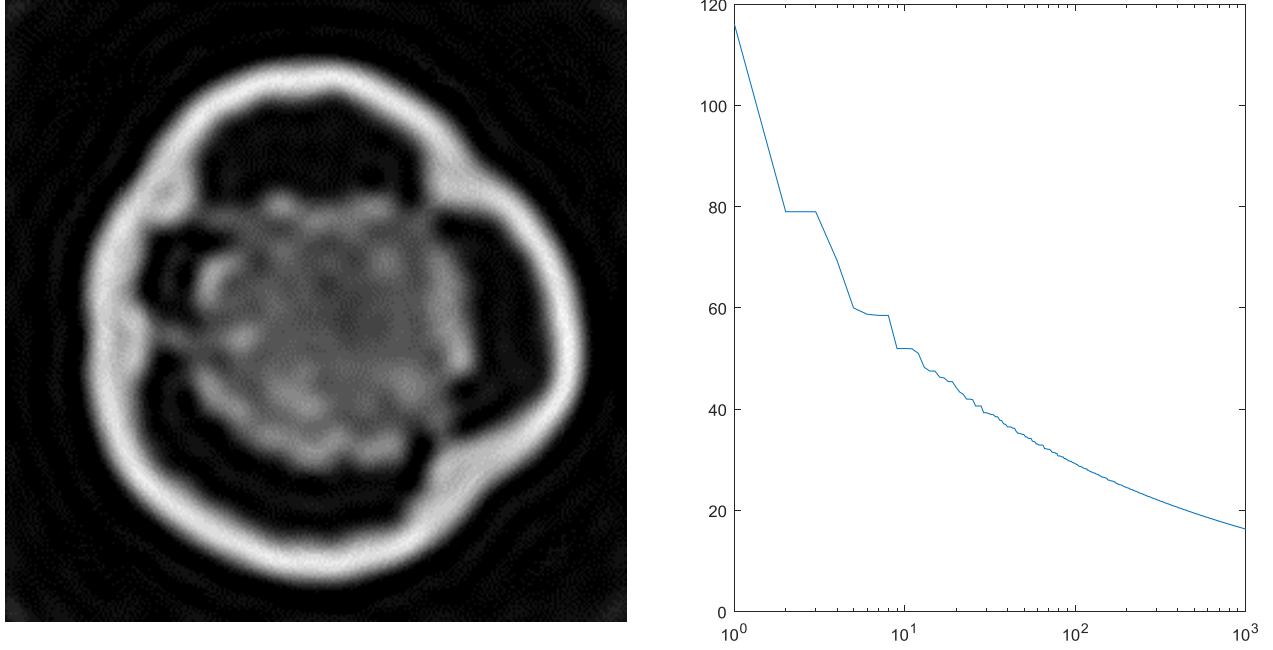


Figure 19. Positive-constrained TSVD image of a pepper slice. Left: image shows severe blurring and ring artifacts. Display window [min max] Right: First 1000 singular values of system matrix

Pseudoinversion and other reconstruction modalities may yield negative pixel values in the image domain. Remediation of negative attenuation coefficients obtained are subject in reconstruction to a positivity constraint, where all  $f_i < 0$  are assigned 0, a nonlinear operation which ostensibly removes the property that  $A^+m$  is a least-squares solution to the system. Small relative residuals from the space of solutions  $f \in \mathbb{R}^+$  may still be obtained by exploiting the similarity of TSVD to Tikhonov regularization (32), where  $\alpha$  is the spectral filtering parameter for the singular values of  $A$  in  $D$ :

$$d_i^{Tikhonov} = \frac{d_i}{d_i^2 + \alpha}. \quad (14)$$

The “best fit” solution is then given by

$$f = \underset{(V D_{filt}^\dagger U^T) m}{\operatorname{argmin}} \left\{ \frac{\|m - A * [(V D_{filt}^\dagger U^T) m]\|_2}{\|m\|_2} \right\}, \quad (15)$$

where  $V$  and  $U$  are components of the SVD and  $D_{filt}^\dagger$  has components given by Equation 14. The tradeoff between data smoothness and quality of fit can be seen in Figure 20.

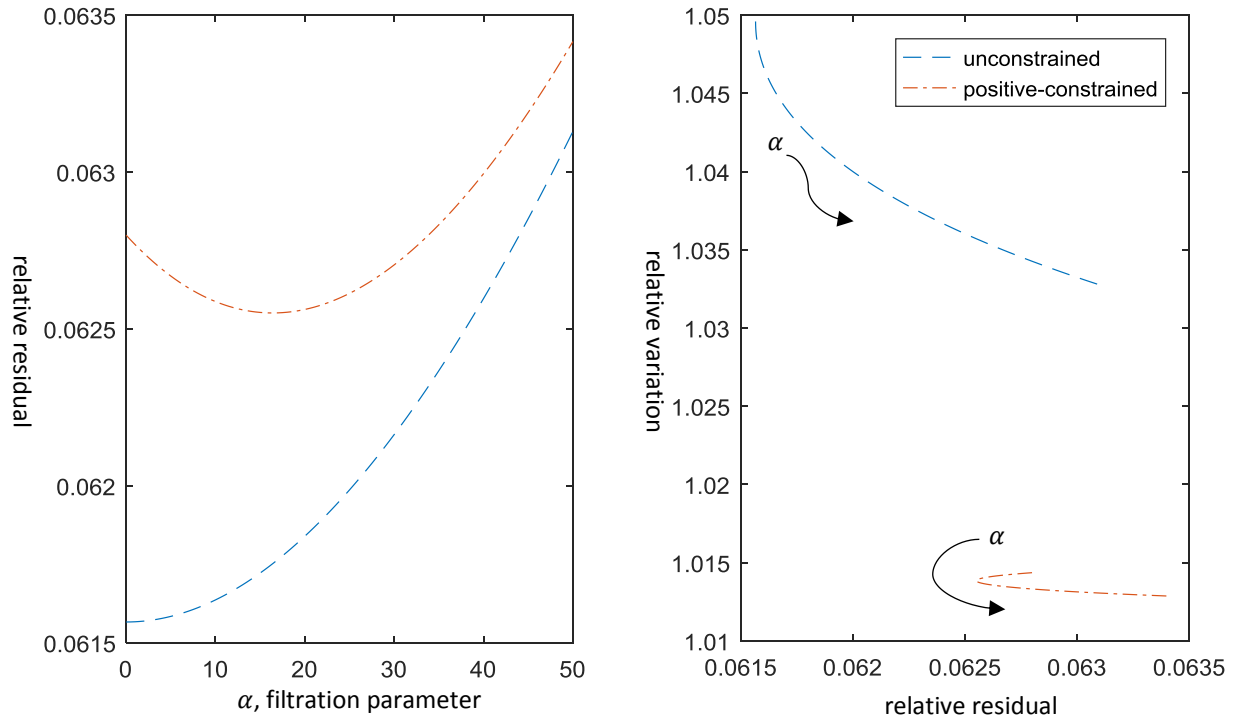


Figure 20. Effect of filtration on TSVD reconstruction of pepper.

#### 4.1.3 Tikhonov and TV regularization

The images in Figure 21 below show images of the same pepper reconstructed via a nonnegative iterative conjugate gradients (ICG) method (45). Tikhonov regularization is accomplished via the penalty functional in

$$f = \operatorname{argmin}_f \{ \|Af - m\|^2 + \alpha \|f\|^2 \}, f \in \mathbb{R}^+ \quad (16)$$

where  $\alpha$  again represents the regularization parameter.

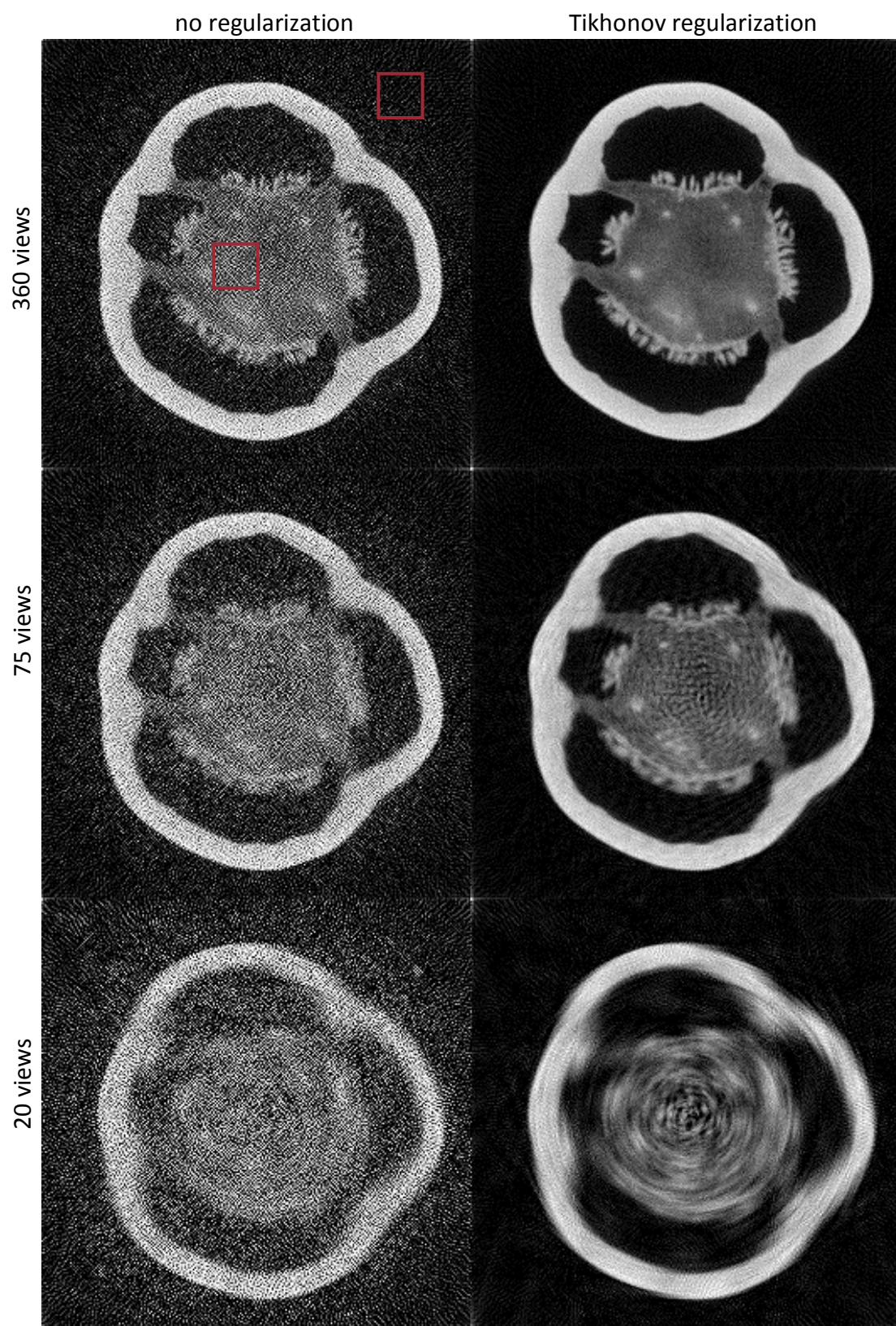


Figure 21. Unregularized vs. Tikhonov-regularized images obtained by ICG. Display windows:  $[0 \ 0.325] \text{ mm}^{-1}$

Figure 22 shows images obtained with a total variation (TV) minimization constraint (46) instead. Since first being proposed by Rudin et al, TV methods for regularization have been the subject of much research (47). TV minimization has edge- and piecewise-constant distribution-preserving properties (48). An image's total variation is defined as

$$V(f) = \sum_{i,j} \sqrt{|f_{i+1,j} - f_{i,j}|^2 + |f_{i,j+1} - f_{i,j}|^2} \quad (17)$$

for an image of  $i \times j$  pixels, with “relative variation” normalized by the total image gray values.

The relevant minimization becomes

$$f = \operatorname{argmin}\{|Af - m| + \xi V(f)\}, f \in \mathbb{R}^+ . \quad (18)$$

Total variation as an image metric loosely characterizes the “smoothness” of a solution – indeed the expressions for TV and noise are superficially similar. Noise standard deviation characterizes the variation between pixels across the image, while TV tracks deviation between individual pixels.

The TV minimization problem is a difficult one to solve, with solution methods taking on various forms (49) (50). Images displayed in Figure 22 are obtained through total variation minimization via a projection onto convex sets (TV-POCS) algorithm (17).



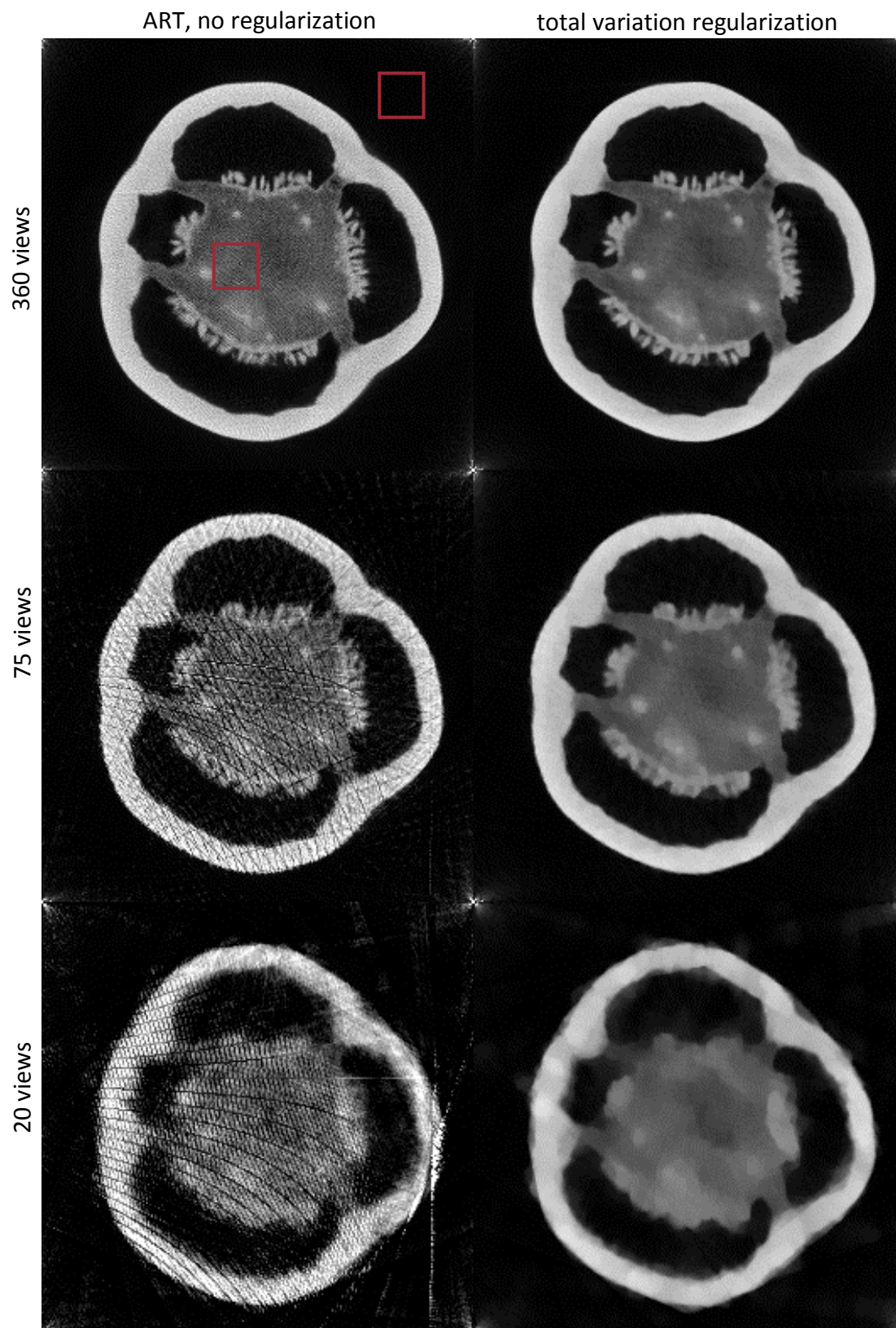


Figure 22. Unregularized vs. TV-regularized images obtained by ART. Display windows:  $[0 \ 0.325] \text{ mm}^{-1}$



## 4.2 Comparison of algorithms

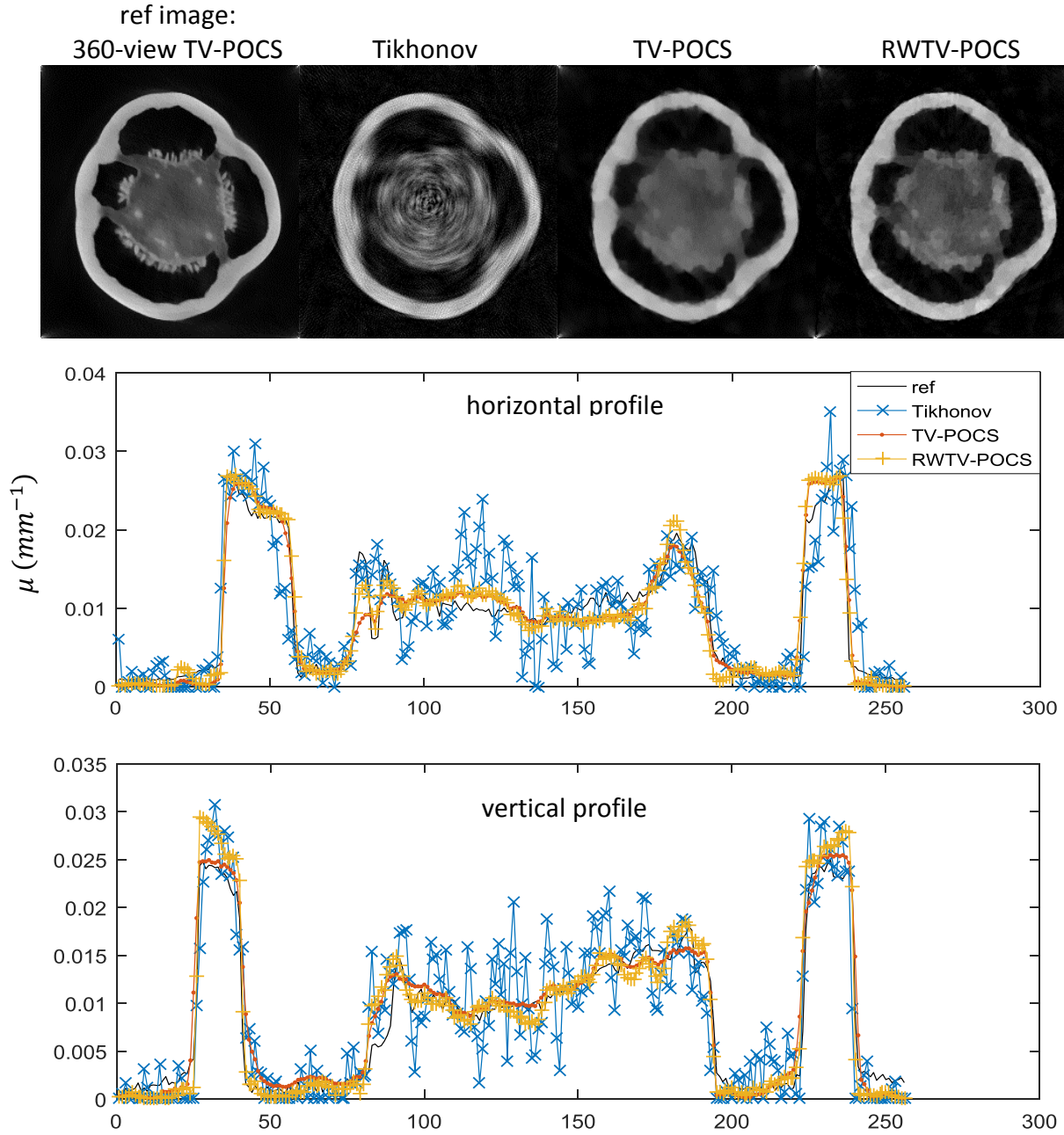


Figure 23. Comparison of algorithms for pepper dataset. Top: 20-view reconstructions using different techniques. Display window  $[[0\ 0.345]\ \text{mm}^{-1}]$ . Middle: Horizontal profiles across center of image. Bottom: Vertical profiles.

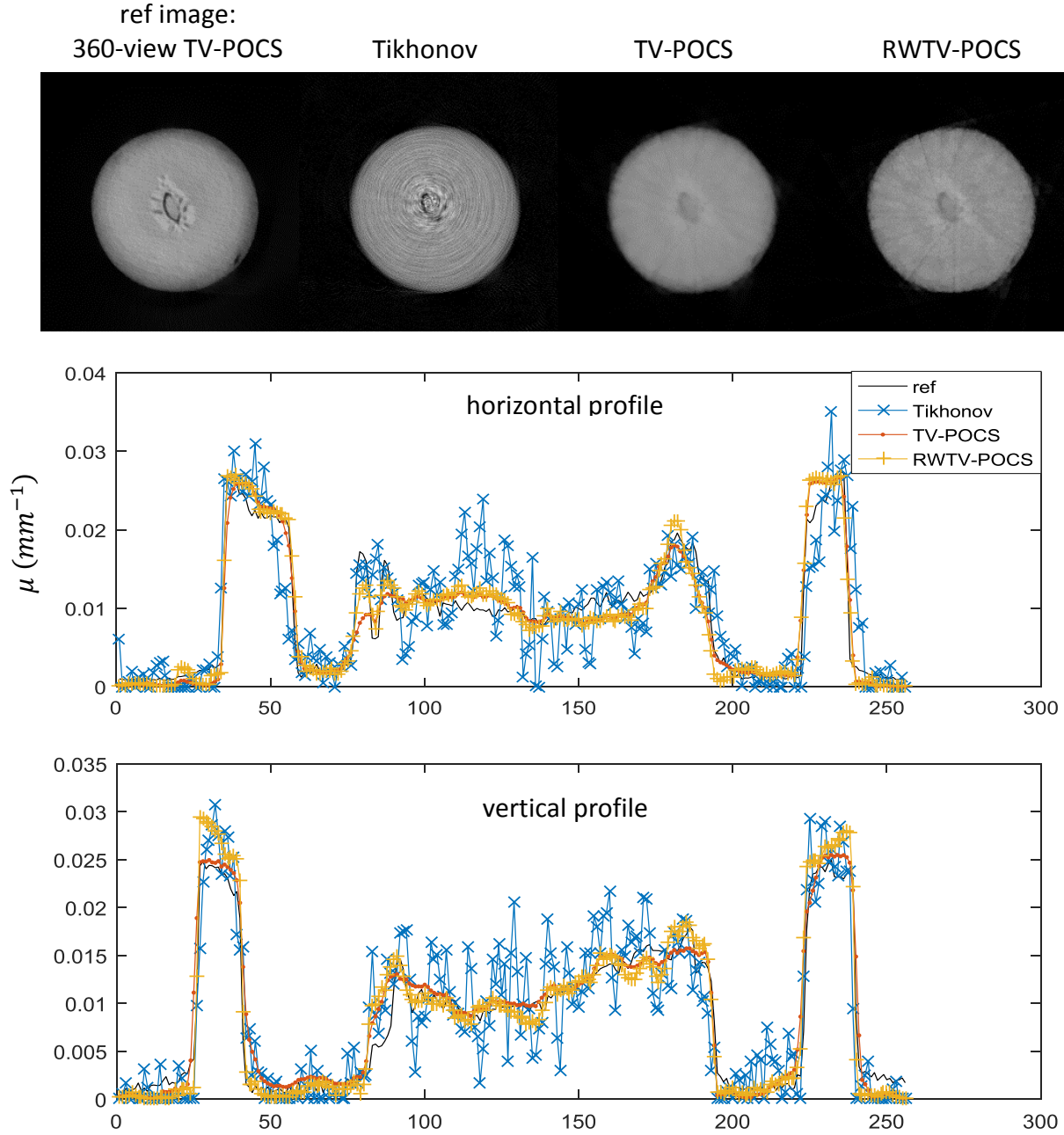


Figure 24. Comparison of algorithms for peach dataset. Top: 20-view reconstructions using different techniques. Display window  $[[0\ 0.2]\text{ mm}^{-1}]$ . Middle: Horizontal profiles across center of image. Bottom: Vertical profiles.

Figure 23 and Figure 24 above show a slice through a pepper and a peach, with 20-view sparse angle reconstruction through various algorithms. The reference images are 360-view images obtained via TV-POCS. Image characteristics are shown below.

Table 5. Image characteristics for Figure 23

<b>pepper, 20 views</b>	<b>ref image</b>	<b>Tikhonov</b>	<b>TV-POCS</b>	<b>RWTV-POCS</b>
<b>SNR</b>	<b>25.8 dB</b>	14.0	22.0	20.0
<b>relative residual</b>	<b>.0573</b>	.0572	.0349	.0338
<b>TV</b>	<b><math>24.5 \text{ mm}^{-1}</math></b>	97.6	12.6	20.9

Table 6. Image characteristics for Figure 24

<b>peach, 20 views</b>	<b>ref image</b>	<b>Tikhonov</b>	<b>TV-POCS</b>	<b>RWTV-POCS</b>
<b>SNR</b>	<b>18.4 dB</b>	9.09	14.8	14.1
<b>relative residual</b>	<b>.0724</b>	.1265	.0647	.0611
<b>TV</b>	<b><math>71.5 \text{ mm}^{-1}</math></b>	227	51.0	70.5

Tikhonov regularization displays high variance on reconstructed data, leading to low SNR and erratic appearance of crossline profiles across images. The TV-POCS and RWTV-POCS reconstructions are very similar, but the extra loop and selection process for the image in RWTV leads as expected to a lower data error than in TV-POCS.

## Chapter 5 – Discussion

---

In this work, previously-known methods for sparse-data reconstruction have been demonstrated on real, noisy datasets acquired on a CT acquisition system which was also designed and constructed as described previously. This system utilizes commercially available components, a rotating object stage, a flat-panel detector, and a microfocus x-ray source, and is capable of acquisition of datasets which, through associated software, may be readily reconstructed to recognizable images. These reconstructions show acceptable image quality parameters including signal-to-noise ratio, and good specificity.

An alternative method for total variation regularization is presented, which is derived from work in (17) (the TV-POCS algorithm) and proposes that in order to maintain a reasonably well-regularized solution to a measurement space which contains detector and radiation random noise, that successive image estimates should be tabulated and their residuals weighted to form the aggregate image, the residual-weighted TV-POCS implementation. As expected, this method underperforms the typical TV-POCS with respect to image signal-to-noise ratio, as well as total variation. It does, however, provide solutions of good fit to the measured data as measured by the relative residual. The residual weighting method nearly matches profiles across the image with reference to a “ground-truth” reconstruction.

The 20-view sampling prevalent in Results (after downsampling) reduces virtual dose to the object by a factor of 18 compared with the 360-view acquisition. In clinical medical practice, the number of views collected about the trajectory of the source and detector may be as high as 1,000 or even higher (51), meaning that higher dose reduction factors may be possible. The amount of dose reduction will naturally be limited by image quality constraints. Even if imaging dose had been reduced by a factor of 5 for half of all patients undergoing necessary CT scans in

2007, the number of potential deaths due to new induced cancers could have been reduced from 14,500 to 5,800 (1).

## Chapter 6 – Conclusion

---

The applicability of regularizing algorithms in sparse-data x-ray CT is promising, with many results suggesting that reconstruction from sparsely sampled data sets is possible while maintaining passable image quality. Sparse-data CT offers advantages over conventional full-data CT reconstruction, with the draw of a lowered collective effective dose to hospital patient populations of particular note. Many methods have been developed for solution of linear inverse problems like that seen in x-ray CT. A few of these methods, demonstrated here, have been shown to be effective at reconstruction of real datasets in addition to having good mathematical foundations as described in the literature. Widespread adoption of sparse-data systems seems unlikely to occur in the near future, but growing concerns over routine imaging dose should eventually lead to a shift toward lowered risk to patients.

## REFERENCES

1. **de Gonzalez, et al.** Projected Cancer Risks From Computed Tomographic Scans Performed in the United States in 2007. *Arch Intern Med.* 2009, Vol. 169(22), pp. 2071-2077.
2. **Korley, FK, Pham, JC and Kirsch, TD.** Use of Advanced Radiology During Visits to US Emergency Departments for Injury-Related Conditions, 1998-2007. *JAMA.* 2010, Vol. 304(13), pp. 1465-1471.
3. **National Council on Radiation Protection and Measurements.** *Report No. 160, Ionizing Radiation Exposure of the Population of the United States.* Bethesda, MD : NCRP, 2009.
4. **Feldkamp, L A, Davis, L C and Kress, J W.** Practical cone-beam algorithm. *Journal of the Optical Society of America.* 1984, Vol. 1, 6, pp. 612-619.
5. **Murphy, M J, et al.** The management of imaging dose during image-guided radiotherapy: Report of the AAPM Task Group 75. *Medical Physics.* 2007, Vol. 34, 10, pp. 4041–4063.
6. **International Commission on Radiological Protection.** 1990 Recommendations of the International Commission on Radiological Protection. *Ann ICRP.* 1991, Vols. 21(1-3), pp. 1-201.
7. **National Council on Radiation Protection and Measurements.** *Limitation of Exposure to Ionizing Radiation.* Bethesda, MD : National Council on Radiation Protection and Measurements, 1993.
8. **Smith-Bindman, Rebecca, et al.** Radiation dose associated with common computed tomography examinations and the associated lifetime attributable risk of cancer. *Archives of internal medicine.* 2009, Vol. 169, 22, pp. 2078-2086.
9. **Mueller, Jennifer L and Siltanen, Samuli (eds.).** *Linear and nonlinear inverse problems with practical applications.* s.l. : SIAM, 2012. ISBN: 978-1-61197-233-7.
10. **Siltanen, Samuli, et al.** Statistical inversion for medical x-ray tomography with few radiographs: I. General theory. *Physics in medicine and biology.* 2003, Vol. 48, 10, p. 1437.
11. **Hamalainen, Keijo, et al.** Sparse tomography. *SIAM Journal on Scientific Computing.* 2013, Vol. 35, 3, pp. B644-B665.
12. **Kalke, Martti and Siltanen, Samuli.** Sinogram interpolation method for sparse-angle tomography. *Applied Mathematics.* 2014, Vol. 5, 03, p. 423.
13. **Liu, Yan, et al.** Adaptive-weighted total variation minimization for sparse data toward low-dose x-ray computed tomography image reconstruction. *Physics in medicine and biology.* 2012, Vol. 57, 23, p. 7923.
14. **Smith, Robert T, et al.** Reconstruction of tomographic images from sparse data sets by a new finite element maximum entropy approach. *Applied optics.* 1991, Vol. 30, 5, pp. 573-582.



15. **Rantala, Maaria, et al.** Wavelet-based reconstruction for limited-angle X-ray tomography. *IEEE transactions on medical imaging*. 2006, Vol. 25, 2, pp. 210-217.
16. **Pan, X, Sidky, E Y and Vannier, M.** Why do commercial CT scanners still employ traditional, filtered back-projection for image reconstruction? *Inverse problems*. 2009, Vol. 25, 12.
17. **Sidky, Emil Y, Kao, Chien-Min and Pan, Xiaochuan.** Accurate image reconstruction from few-views and limited-angle data in divergent-beam CT. *Journal of X-ray Science and Technology*. 2006, Vol. 14, 2, pp. 119-139.
18. **Shepp, Larry A and Logan, Benjamin F.** The Fourier Reconstruction of a Head Section. *IEEE Transactions on Nuclear Science*. 1974, Vol. 21, 3, pp. 21-43.
19. **Sidky, Emil Y and Pan, Xiaochuan.** Image reconstruction in circular cone-beam computed tomography by constrained, total-variation minimization. *Physics in medicine and biology*. 2008, Vol. 53, 17, p. 4777.
20. **Berger, M J, et al.** *XCOM: Photon Cross Section Database (version 1.5)*. [Online] s.l. : NIST, 2010.
21. **Johnson, Thorsten RC and et al.** Material differentiation by dual energy CT: initial experience. *European radiology*. 2007, Vol. 17, 6, pp. 1510-1517.
22. **Siddon, R L.** Fast calculation of the exact radiological path for a three-dimensional CT array. *Medical Physics*. Vol. 12, pp. 252-255.
23. **Ambartsumian, R.** A life in astrophysics. Selected paper of Viktor A. Ambartsumian. *Astrophysics*. Vol. 41, 4, pp. 328-330.
24. **Hadamard, J.** Sur les Problemes Aux Derivees Partielles et Leur Signification Physique. *Princeton University Bulletin*. 1902, pp. 49-52.
25. **Radon, Johann.** Über die Bestimmung von Funktionen durch ihre Integralwerte längs gewisser Mannigfaltigkeiten. *Berichte über die Verhandlungen der Königlich-Sächsischen Akademie der Wissenschaften zu Leipzig, Mathematisch-Physische Klasse*. 1917, 69, pp. 262-277.
26. **Bracewell, R N.** Strip integration in radio astronomy. *Australian Journal of Physics*. 1956, Vol. 9, pp. 198-217.
27. **Blackman, R B and Tukey, J W.** Particular pairs of windows. *The measurement of power spectra, from the point of view of communications engineering*. 1959, pp. 95-101.
28. **Oppenheim, A V, Schafer, R W and Buck, J R.** *Discrete-Time Signal Processing*. Upper Saddle River, NJ : Prentice Hall, 1999. ISBN: 0131988425.

29. **Kohler, Th, et al.** Artifact analysis of approximate helical cone-beam CT reconstruction algorithms. *Medical Physics*. 2002, Vol. 29, 1, pp. 51-64.
30. **Taguchi, Katsuyuki, Chiang, Be-Shan S and Silver, Michael D.** A new weighting scheme for cone-beam helical CT to reduce the image noise. *Physics in Medicine and Biology*. 2004, Vol. 49, 11, p. 2351.
31. **Tang, X, et al.** A three-dimensional-weighted cone beam filtered backprojection (CB-FBP) algorithm for image reconstruction in volumetric CT—helical scanning. *Phys Med Biol*. 2006, Vol. 51, 4, pp. 855-874.
32. **Hansen, Per Christian.** The truncated SVD as a method for regularization. *BIT Numerical Mathematics*. 1987, Vol. 27, 4, pp. 534-553.
33. **Hansen, Per Christian, Nagy, James G and O'leary, Dianne P.** *Deblurring images: matrices, spectra, and filtering*. s.l. : Society for Industrial and Applied Mathematics, 2006. ISBN: 978-0-898716-18-4.
34. **Horn, Roger A and Johnson, Charles R.** *Matrix analysis*. s.l. : Cambridge UP, 2012. ISBN: 0521548233 .
35. —. *Topics in matrix analysis*. s.l. : Cambridge UP, 1994. ISBN: 0521548233.
36. **Kaczmarz, Stefan.** Angenäherte Auflösung von Systemen linearer Gleichungen. *Bulletin International de l'Académie Polonaise des Sciences et des Lettres*. 1937, Vol. A, 35, pp. 355-357.
37. **Gordon, R, Bender, R and Herman, G T.** Algebraic Reconstruction Techniques (ART) for Three-dimensional Electron Microscopy and X-ray Photography. *Journal of theoretical Biology*. 1970, Vol. 29, pp. 471-481.
38. **Pratx, G, et al.** Fast, Accurate and Shift-Varying Line Projections for Iterative Reconstruction Using the GPU. *IEEE transactions on medical imaging*. 2009, Vol. 28, 3, pp. 435-445.
39. **Jia, X, et al.** GPU-based iterative cone-beam CT reconstruction using tight frame regularization. *Physics in Medicine & Biology*. 2011, Vol. 56, 13, p. 3787.
40. **Byunghyun, J, et al.** Multi GPU implementation of iterative tomographic reconstruction algorithms. *Biomedical Imaging: From Nano to Macro*. ISBI'09, 2009.
41. **Wei, X and Mueller, K.** A performance-driven study of regularization methods for gpu-accelerated iterative ct. *Workshop on High Performance Image Reconstruction*. (HPIR), 2009.
42. **Deng, Junjun.** *Parallel computing techniques for computed tomography*. PhD (Doctor of Philosophy) thesis : University of Iowa, 2011.

43. **Webb, Andrew G.** *Introduction to Biomedical Imaging*. Hoboken : Wiley-IEEE, 2002. ISBN: 978-0-471-23766-2.
44. **Fessler, Jeffrey A.** Michigan image reconstruction toolbox. [Online] [Cited: June 1, 2017.] <https://web.eecs.umich.edu/~fessler/code/>.
45. **Hestenes, Magnus R and Stiefel, Eduard.** Methods of Conjugate Gradients for Solving Linear Systems. *Journal of Research of the National Bureau of Standards*. 1952, Vol. 49, 6.
46. **Rudin, Leonid I, Osher, Stanley and Fatemi, Emad.** Nonlinear total variation based noise removal algorithms. *Physica D: Nonlinear Phenomena*. 1992, 60, pp. 1-4.
47. **Wolfgang, Stefan.** *Total variation regularization for linear ill-posed inverse problems: Extensions and applications*. s.l. : Arizona State University, 2008.
48. **Strong, David and Chan, Tony.** Edge-preserving and scale-dependent properties of total variation regularization. *Inverse problems*. 2003, Vol. 19, 6, p. S165.
49. **Chan, Tony F, Golub, Gene H and Mulet, Pep.** A nonlinear primal-dual method for total variation-based image restoration. *SIAM journal on scientific computing*. 1999, Vol. 20, 6, pp. 1964-1977.
50. **Goldstein, Tom and Osher, Stanley.** The split Bregman method for L1-regularized problems. *SIAM journal on imaging sciences*. 2009, Vol. 2, 2, pp. 323-343.
51. **Goldman, Lee W.** Principles of CT and CT technology. *Journal of nuclear medicine technology*. 2007, Vol. 35, 3, pp. 115-128.